Extending the Effective Temperature Model to the Large Strain Hardening Behavior of Glassy Polymers*

Zheliang Wang[a], Jingkai Guo[a], Jonathan E. Seppala[c], Thao D. Nguyen[a,b,*]

[a]*Department of Mechanical Engineering, The Johns Hopkins University, Baltimore, MD 21218, USA*
[b]*Department of Materials Science and Engineering, The Johns Hopkins University, Baltimore, MD 21218, USA*
[c]*Materials Science and Engineering Division, National Institute of Standards and Technology, Gaithersburg, MD 20899, USA*

Abstract

Amorphous polymers exhibit a viscoplastic strain hardening behavior at large strains. To describe this hardening behavior, we have developed an effective temperature model for the nonequilibrium behavior of amorphous polymers that incorporate the effects of network orientation and relaxation at large plastic deformation. The development of network orientation is introduced as a backstress that produces kinematic hardening in the stress response, while network relaxation describes the effects of temperature and strain rate on the hardening response. The model was applied to simulate the thermomechanical behavior of polycarbonate (PC) to determine the model parameters from standard dynamic frequency sweep and differential scanning calorimetry tests. The simulation results showed that the model can quantitatively capture the dependence of the hardening modulus on strain, strain rate, and temperature, as well as the unloading and reloading behavior measured in uniaxial compression tests. We applied the model to investigate the effect of plastic dissipation on the peeling of a polymer filament from a rigid substrate to guide the design of peel tests to measure the intrinsic fracture toughness of polymers fabricated by melt extrusion additive manufacturing processes.

Keywords: Strain hardening, Network relaxation, Effective temperature, Finite element, Thermodynamics, Peel

1. Introduction

The post-yield behavior of glassy polymers is characterized by strain-softening followed by strain-hardening that can produce a dramatic upswing in the stress-strain curve at large strains. The degree of hardening varies between different polymers and can determine whether the material fails by brittle or ductile mechanisms. The initial strain-softening response can be attributed to a decrease in the resistance to local rearrangements of polymer chain segments caused by the disordering effects of plastic deformation. The yield stress and the post-yield stress drop increase at lower temperatures, higher strain rates and longer annealing times. Likewise, the strain-hardening modulus increases with lower temperatures and higher strain rates [1, 2, 3, 4, 5, 6, 7].

The temperature- and rate-dependence of the yield stress has been captured by the Eyring model [8, 9] for stress-activated viscous flow [7] and various microstructurally motivated models, such as the double kink model of Argon [10] and the shear transformation zone model of Hasan and Boyce [11]. The post-yield stress drop is commonly described by the evolution of the Eyring activation stress, or an analogous microstructural variable, with the plastic strain rate, while physical aging is similarly described by the static recovery of the activation stress and analogous microstructural variables [12, 13, 14]. An alternative approach, developed by Buckley and coworkers [15, 16] and Xiao and Nguyen [17, 18, 19, 20, 21], applies the effective temperature thermodynamic theory to connect the post-yield stress drop and physical aging to the evolution of a nonequilibrium configurational structure. The effective temperature theory splits the degrees of freedom of amorphous polymers into a kinetic subsystem that equilibrates instantaneously

*Corresponding author
Email address: Vicky.Nguyen@jhu.edu (Thao D. Nguyen)

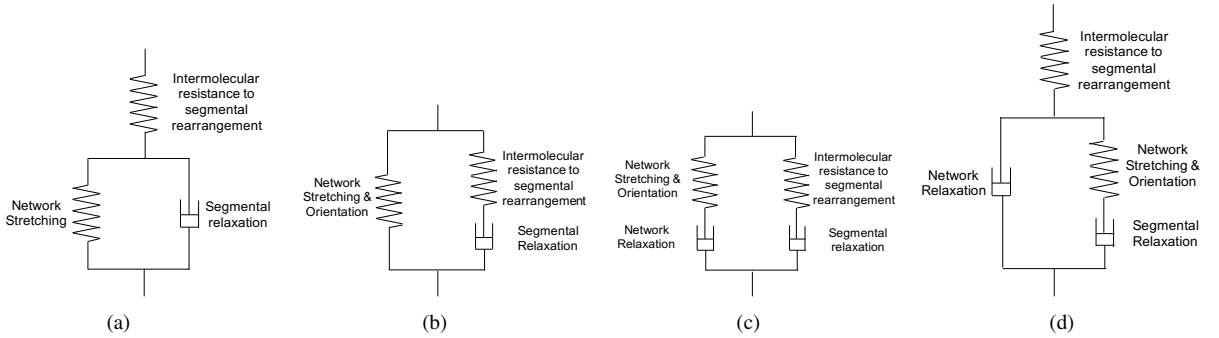

Figure 1: One dimensional rheological representations of constitutive models for the large deformation viscoplastic behavior of amorphous polymers developed by (a)Haward and Thackray [25], (b) Bergstrom et. al. [36], Goavaert et. al. [37], and Buckley et. al. [38]. (c) Dupaix et. al. [39] (d) Hempel [40] and the present work

with the temperature and a slowly-evolving configurational subsystem characterized by an effective temperature. Heat transfer between the kinetic and configurational subsystems drives the effective temperatures towards equilibrium over time, while plastic deformation disorders the structure, driving it away from equilibrium. In Xiao and Nguyen [19], this process was coupled to viscoplastic deformation using the nonlinear Adam-Gibbs [22, 23] theory to describe the effect of the nonequilibrium configurational structure on the viscous resistance to plastic deformation. This allowed the model to explain a wide range of temperature-dependent and time-dependent phenomena, including physical aging and mechanical rejuvenation, on the stress response through post-yield softening [19, 14, 24].

The goal of this work was to extend the Xiao and Nguyen [19] model to describe the strain-hardening behavior of glassy polymers at large strains. The hardening behavior of glassy polymers is attributed to the stretching and development of long-range orientation of the entangled polymer network. Haward and Thackray [25] first modeled strain hardening as an entropy-elasticity mechanism and developed a nonlinear rheological model consisting of a spring for the initial linear elastic response in series with a Voigt element for the viscoplastic response. The Voigt element includes an Eyring dashpot for the intermolecular resistance to yield and viscous flow in parallel with a spring for the entropy change of the entangled network with deformation. For uniaxial tension, the entropic hardening stress can be derived as, $\sigma_H = -\lambda T(\frac{\partial \eta}{\partial \lambda})_T$, where λ is the axial stretch, η is the entropy per unit volume, σ_H is the true stress and T is the temperature. Assuming that the chains obey Gaussian statistics yields the Gaussian hardening model,

$$\sigma_H(\lambda) = G_R(\lambda^2 - 1/\lambda), \tag{1}$$

where G_R is defined as the hardening modulus [26]. Haward and Thackray used a Langevin statistical model for an oriented polymer chain instead of the Gaussian approximation to describe the dramatic increase in the hardening modulus near the limit of chain extensibility [27, 28]. Molecular dynamics simulations have shown that the transition between Gaussian hardening and Langevin hardening strongly depends on the entanglement density [5]. The model has been generalized to three-dimensions by replacing the Langevin spring with rubber elasticity models [29, 30, 31, 32, 33, 34] including the 8-chain network model [28] and the full-chain model [35].

In the Voigt arrangement (Fig. 1a), the entropic spring functions as a nonlinear backstress that produces a strong Bauschinger effect upon unloading [30] and an anisotropic yield and post-yield stress response in cold-worked polymers [41]. Subsequent constitutive developments replaced the backstress with an equilibrium stress (Fig. 1b) [36, 37, 38]. The two formulations can reproduce the same features of the stress-strain curves during loading, but elastic hardening cannot capture the Bauschinger effect at large strains and can erroneously produce yielding during unloading [42]. Experiments and molecular dynamics studies have also revealed significant inconsistencies in the entropic model for strain hardening. Entropic elastic hardening models produce the opposite temperature trend than observed experimentally. Moreover, the hardening modulus is orders of magnitude larger than the modulus calculated from the entanglement density [4, 25, 26].

To produce the negative temperature dependence of the hardening modulus, various studies have modified the temperature dependence of network models to account for the loss of entanglements at higher temperatures [6, 43].

However, this approach can lead to unphysical stress response in a constrained cooling and heating cycle [40]. More recent studies have incorporated a molecular relaxation mechanism for the network chains to describe the temperature dependence and rate-dependence of the hardening modulus [44, 39, 45]. Boyce and coworkers replaced the entropic elastic hardening model with the Bergstrom-Boyce [36] model, developed for the nonlinear viscoelastic behavior of elastomers, to describe the effects of network deformation relaxation in glassy and semicrystalline polymers. Hempel incorporated the network relaxation into the original formulation of Haward and Thackray by replacing the entropic spring with a Maxwell fluid element (Fig. 1c). An evolution law inspired by the work of Bergstrom-Boyce was proposed for the network relaxation to capture the effects of temperature, strain, and strain rate on the hardening response. The authors showed that the viscous backstress model produced a more physical stress response than the athermal backstress and temperature-dependent backstress [6, 43], models to a complex thermomechanical history. [40]

In this paper, we developed a model for the large deformation viscoplastic behavior of amorphous polymers by incorporating the rate-dependent backstress formulation for network orientation and relaxation (Fig. 1d) into the Xiao and Nguyen [19] effective temperature model, to capture the temperature-dependent and strain-rate dependent post-yield strain-hardening behavior and the Bauschinger effect under reversed loading. A relaxation spectrum is applied to more accurately describe the post-yield rate-dependent response over a wide range of temperatures below the glass transition temperature. The constitutive model was applied to simulate the uniaxial compression response of a polycarbonate (PC) material used for fused filament fabrication (FFF), a widely used polymer melt extrusion process for 3D printing. Results showed that the model was able to accurately capture the strain hardening behavior, unloading and reloading behavior over a wide range of strain rates and temperatures. The model was then applied to simulate the peeling of PC fibers to investigate the effects of the post-yield softening and hardening response on the peel energy and intrinsic plastic dissipation. The findings provide insights for the design of peel tests to measure the weld strength of FFF printed fibers.

2. Methods

2.1. Experimental methods

2.1.1. Materials and specimen preparation

Polycarbonate (PC) fibers with a molecular mass of $M_n = 1.671 \times 10^4$ g/mol and a fiber diameter of (2.85 ± 0.05) mm were purchased from Ultimaker[1] (Watermolenweg 2, 4191PN, Geldermalsen, The Netherlands). The fibers were cut into cylindrical specimens with an average length of 4 mm for uniaxial compression tests. The cut surfaces were polished with sandpaper. Thin film specimens were processed by melting the PC fibers at 200 °C and injecting the melt into a square steel mold of lengths 50.0 mm and thickness 2.0 mm then cooling to room temperature on the counter. The film was cut into 20.0 mm × 5.0 mm × 2.0 mm strips specimens with a band saw for dynamic mechanical testing.

2.1.2. Dynamic frequency sweep tests

We used a previously developed method [46, 18, 19] to characterize the stress relaxation spectrum of the PC material. Dynamic frequency sweep tests were performed using a TA Q800 Dynamic Mechanical Analyzer (DMA), whose manufacturer rated resolution is 0.0001 N and 1 nm. Thin film specimens, described in Sec. 2.1.1, were mounted between the tensile grips with a gauge length of 10 mm. The specimens were subjected to stepwise temperature increases from 35 °C to 143 °C in 2 °C increments in air. At each temperature, a dynamic strain of 0.2 % amplitude was applied at 0.32 Hz, 1.0 Hz, 3.2 Hz, 10.0 Hz, and 31.6 Hz to measure the storage modulus $G(\omega, T)$. Applying the time-temperature superposition (TTS) principle for thermorheologically simple materials, the storage modulus at different temperatures were shifted to the reference temperature $T_0 = 143$ °C to obtain the master curve of the frequency response [47]. The resulting temperature dependent shift factor $a(T)$ in the glass transition temperature range was used

[1] Certain commercial equipment, instruments, or materials are identified in thispaper in order to specify the experimental procedure adequately. Such identificationis not intended to imply recommendation or endorsement by the National Insti-tute of Standards and Technology, nor is it intended to imply that the materials orequipment identified are necessarily the best available for the purpose.

to determine the parameters of the Williams-Landel-Ferry (WLF) equation,

$$\log a_T(T) = \frac{-C_1^0(T-T_0)}{C_2^0+T-T_0}, \tag{2}$$

where C_1^0 and C_2^0 are the WLF constants at the reference temperature T_0. The WLF constants can be shifted to T_g as $C_2^g = C_2^0 + T_g$ and $C_1^g C_2^g = C_1^0 C_2^0$ [47].

2.1.3. Differential scanning calorimetry

Differential scanning calorimetry (DSC) measurements were performed to determine the heat capacity of polycarbonate below and above glass transition temperature as well as the structural relaxation spectrum. Specimens weighing 8.9 mg were cut from the PC fiber and put in a TA Q20 DSC. The manufacturer rated precision for TA Q20 was ± 0.1 °C. The specimens were equilibrated at 150 °C for 30 mins to remove the thermal history then cooled to 88 °C at 3 °C/min and annealed for 24 h. The annealed specimens were cooled to 20 °C at 3 °C/min and then heated to 250 °C at 5 °C/min to measure the heat flow rate.

2.1.4. Uniaxial compression

Uniaxial compression tests at constant temperatures were performed to measure the strain hardening behavior of the polycarbonate. Cylindrical specimens with dimensions specified in Sec. 2.1.1 were equilibrated at 143 °C and annealed 30 mins to erase the thermal history. The specimens were cooled at 3 °C/min to the test temperatures, 95 °C, 37 °C, 27 °C or 15 °C and annealed at the test temperature for 30 mins in an incubator (Ecotherm, Hartkirchen, Austria). The annealed specimens were placed in an MTS Insight 5 electromechanical testing system (Eden Prairie, MN, USA) equipped with an environmental temperature chamber (Thermcraft, Inc. Winston Salem, NC, USA), set at the test temperature, and subjected to compressive loading to 100 % true strain at true strain rates 10^{-3}/s, 10^{-4}/s, and 10^{-5}/s. Three tests were performed at each strain rate and temperature to ensure repeatability. To measure the material response to unloading and reloading, another set of specimens were first compressed at room temperature (27 °C) to 60 % true strain at an engineering strain rate of 10^{-3}/s or 10^{-4}/s, unloaded to zero force at the same strain rate and reloaded to 100 % true strain at the same strain rate.

2.2. Constitutive model

2.2.1. Kinematics

Consider a deformation $\mathbf{x} = \boldsymbol{\varphi}(\mathbf{X})$ that maps points $\mathbf{X}$ in the reference configuration Ω_0 to points $\mathbf{x}$ in the spatial configuration Ω. The deformation gradient is defined as $\mathbf{F} = \frac{\partial \boldsymbol{\varphi}}{\partial \mathbf{X}}$ and maps material lines $\mathrm{d}\mathbf{X} \in \Omega_0$ to spatial lines $\mathrm{d}\mathbf{x} \in \Omega$. To model the rate-dependent yield and viscous flow response, we assumed a multiplicative split of the deformation gradient into elastic and and viscous parts,

$$\mathbf{F} = \mathbf{F}^e \mathbf{F}^v \tag{3}$$

The viscous part $\mathbf{F}^v$ represents the local rearrangements of polymer segments that give rise to the rate-dependent yield and viscoplastic deformation. The elastic and viscous deformation gradients can be decomposed further into a stretch and rotation by polar decomposition, $\mathbf{F}^e = \mathbf{R}^e\mathbf{U}^e = \mathbf{V}^e\mathbf{R}^e$ and $\mathbf{F}^v = \mathbf{R}^v\mathbf{U}^v = \mathbf{V}^v\mathbf{R}^v$. This allows the deformation gradient to be expressed as $\mathbf{F} = \mathbf{V}^e\mathbf{R}\mathbf{U}^v$, where $\mathbf{R} = \mathbf{R}^e\mathbf{R}^v$ is the rotation [30]. We choose to assign all of the rotation to the viscous deformation, $\mathbf{R}^v = \mathbf{R}$ and $\mathbf{R}^e = \mathbf{I}$, which results in a symmetric elastic deformation gradient $\mathbf{F}^e = \mathbf{V}^e$[28].

To model strain hardening and relaxation, the viscous deformation gradient is further decomposed multiplicatively into two components,

$$\mathbf{F}^v = \mathbf{F}^{ne}\mathbf{F}^{nv}. \tag{4}$$

The elastic network deformation $\mathbf{F}^{ne}$ is the recoverable part of $\mathbf{F}^v$ arising from the resistance to the stretching of network chains and $\mathbf{F}^{nv}$ is the unrecoverable part caused by the relaxation of the network chains. The sequence of deformation maps generated by the successive decompositions of the deformation gradient is illustrated in Fig. 2(a). The viscous deformation gradient $\mathbf{F}^v$ describes an intermediate configuration $\hat{\Omega}$ resulting from the instantaneous unloading from the current configuration, while $\mathbf{F}^{nv}$ describes an intermediate configuration $\widetilde{\Omega}$ obtained by instantaneous

unloading by the total elastic deformation gradient $\widetilde{\mathbf{F}}^e = \mathbf{F}^e\mathbf{F}^{ne}$. Applying the polar decomposition, the viscous deformation gradient can be expressed as $\mathbf{F}^v = \mathbf{V}^{ne}\mathbf{R}^v\mathbf{U}^{nv}$, where $\mathbf{R}^v = \mathbf{R}^{ne}\mathbf{R}^{nv}$. We choose to assign all of the rotation to the network viscous tensor, $\mathbf{R}^{nv} = \mathbf{R}^v = \mathbf{R}$, which causes $\mathbf{R}^{ne} = \mathbf{I}$ and $\mathbf{F}^{ne} = \mathbf{V}^{ne}$. Furthermore, we can show that the total elastic deformation gradient $\widetilde{\mathbf{F}}^e = \mathbf{F}^e\mathbf{F}^{ne}$ is symmetric and $\mathbf{F}^e$ is coaxial with $\mathbf{F}^{ne}$. The total deformation gradient can be expressed as, $\mathbf{F} = \widetilde{\mathbf{V}}^e\widetilde{\mathbf{R}}^e\mathbf{R}^{nv}\mathbf{U}^{nv}$. However, $\widetilde{\mathbf{R}}^e = \mathbf{I}$, because $\mathbf{R}^{nv} = \mathbf{R}$, thus $\mathbf{F}^e\mathbf{F}^{ne} = \widetilde{\mathbf{V}}^e$. Then, $\mathbf{F}^e\mathbf{F}^{ne} = \left(\mathbf{F}^e\mathbf{F}^{ne}\right)^T = \mathbf{F}^{ne^T}\mathbf{F}^{e^T} = \mathbf{F}^{ne}\mathbf{F}^e$, which shows that $\mathbf{F}^e$ is coaxial with $\mathbf{F}^{ne}$. These assumptions will significantly simplify the constitutive formulation for the rate of the viscous deformations in the following developments. Boyce et al. [30] compared three constitutive assumptions for the internal rotation, including the $\mathbf{R}^v = \mathbf{R}$ applied here, and showed that they had no effect on the elastic kinematic hardening model developed by Boyce et al. for glassy polymers.

The right and left Cauchy-Green deformation tensors for $\mathbf{F}$, $\mathbf{F}^e$ and $\mathbf{F}^{n,e}$ are defined as,

$$\begin{aligned} \mathbf{C} &= \mathbf{F}^T\mathbf{F}, \quad \mathbf{C}^e = \mathbf{F}^{e^T}\mathbf{F}^e, \quad \mathbf{C}^{ne} = \mathbf{F}^{ne^T}\mathbf{F}^{ne} \\ \mathbf{b} &= \mathbf{F}\mathbf{F}^T, \quad \mathbf{b}^e = \mathbf{F}^e\mathbf{F}^{e^T}, \quad \mathbf{b}^{ne} = \mathbf{F}^{ne}\mathbf{F}^{ne^T}. \end{aligned} \tag{5}$$

The spatial velocity gradient and inelastic counterparts in the intermediate configurations $\hat{\Omega}$ and $\widetilde{\Omega}$ are defined respectively as,

$$\mathbf{L} = \dot{\mathbf{F}}\mathbf{F}^{-1}, \quad \mathbf{L}^v = \dot{\mathbf{F}}^v\mathbf{F}^{v^{-1}}, \quad \mathbf{L}^{nv} = \dot{\mathbf{F}}^{nv}\mathbf{F}^{nv^{-1}}. \tag{6}$$

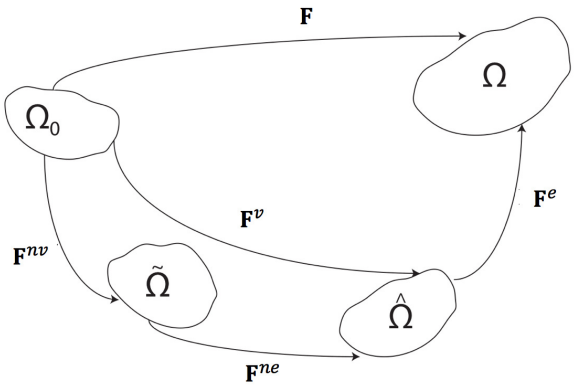

(a)

Figure 2: Decomposition scheme for the deformation gradient.

2.2.2. Effective temperature thermodynamic theory

In the effective temperature thermodynamic theory, the internal energy and entropy of an amorphous material can be decomposed into contributions from two weakly interacting subsystems. [48, 49, 50, 19] The kinetic subsystem contains fast processes, such as vibrational motion, that equilibrate instantaneously with the thermal reservoir at a temperature T. The configurational subsystem contains slow processes, such as configurational arrangements, that are in quasi-equilibrium at an effective temperature T_e. Each thermodynamic subsystem is characterized by an internal energy density, entropy density, heat flux and entropy flux, and these sum to provide the total internal energy density $e = e^k + e^c$, entropy density $\eta = \eta^k + \eta^c$, heat flux $\mathbf{Q} = \mathbf{Q}^k + \mathbf{Q}^c$ and entropy flux $\mathbf{H} = \mathbf{H}^k + \mathbf{H}^c$ of the system. The entropy flux of the kinetic and configurational subsystems are defined using the characteristic temperature of the system, $\mathbf{H}^k = \mathbf{Q}^k/T$ and $\mathbf{H}^c = \mathbf{Q}^c/T_e$ [48]. It follows that the Helmholtz free energy density can be additively decomposed into kinetic and configurational contributions [49],

$$\Psi = \Psi^k + \Psi^c = (e^k - T\eta^k) + (e_i^c - T_e\eta^c), \tag{7}$$

In general, the free energy density $\Psi(T, T_e, \mathbf{C}, \mathbf{C}^e, \mathbf{C}^{ne})$ depends on the temperature, effective temperature, deformation, and internal variables for inelastic deformations. Formulating the Ψ in terms of the Lagrangian deformation tensors $\mathbf{C}$, $\mathbf{C}^e$ and $\mathbf{C}^{ne}$ ensures objectivity in the current and intermediate configurations.

The first law of thermodynamics in the reference configuration can be written as,

$$\dot{e} = \mathbf{S} : \frac{1}{2}\dot{\mathbf{C}} - \nabla_{\mathbf{X}} \cdot \mathbf{Q}, \tag{8}$$

where $\mathbf{S}$ is the second Piola-Kirchhoff stress tensor, e is the internal energy density and $\mathbf{Q}$ is the heat flux. The second law of thermodynamics can be written in the reference configuration as,

$$\dot{\eta} + \nabla_{\mathbf{X}} \cdot \mathbf{H} \geq 0, \tag{9}$$

where η is the entropy density and $\mathbf{H}$ is the entropy flux. The decomposition of the Helmholtz free energy density eq. (7) can be applied to eqs. (8) and (9) to rewrite the first and second laws in terms of $\dot{\Psi}$ as,

$$\dot{e^k} + \dot{e^c} = \mathbf{S} : \frac{1}{2}\dot{\mathbf{C}} - \nabla_{\mathbf{X}} \cdot \mathbf{Q}^k - \nabla_{\mathbf{X}} \cdot \mathbf{Q}^c, \tag{10}$$

$$(T - T_e)\,\dot{\eta}^c + (T - T_e)\,\frac{\nabla_{\mathbf{X}} \cdot \mathbf{Q}^c}{T_e} - \frac{1}{T}\mathbf{Q}^k \cdot \nabla_{\mathbf{X}} T - \frac{T}{T_e^2}\mathbf{Q}^c \cdot \nabla_{\mathbf{X}} T_e + \mathbf{S} : \frac{1}{2}\dot{\mathbf{C}} - \dot{T}\eta^k - \dot{T}_e \eta^c - \dot{\Psi} \geq 0. \tag{11}$$

Expanding $\dot{\Psi}$ gives,

$$\dot{\Psi} = \frac{\partial \Psi}{\partial T}\dot{T} + \frac{\partial \Psi}{\partial T_e}\dot{T}_e + 2\frac{\partial \Psi}{\partial \mathbf{C}} : \frac{1}{2}\dot{\mathbf{C}} + \frac{\partial \Psi}{\partial \mathbf{C}^e} : \dot{\mathbf{C}}^e + \frac{\partial \Psi}{\partial \mathbf{C}^{ne}} : \dot{\mathbf{C}}^{ne}, \tag{12}$$

The rate of the elastic deformation tensors can be written as, $\dot{\mathbf{C}}^e = \mathbf{F}^{v^{-T}}\dot{\mathbf{C}}\mathbf{F}^{v^{-1}} - 2\mathrm{sym}\left[\mathbf{C}^e\mathbf{L}^v\right]$ and $\dot{\mathbf{C}}^{ne} = \mathbf{F}^{ne^T}\mathrm{sym}\left[\mathbf{L}^v\right]\mathbf{F}^{ne} - 2\mathrm{sym}\left[\mathbf{C}^{ne}\mathbf{L}^{nv}\right]$. Applying these relations to eq. (12) and rearranging terms give,

$$\dot{\Psi} = \frac{\partial \Psi}{\partial T}\dot{T} + \frac{\partial \Psi}{\partial T_e}\dot{T}_e + \left(2\frac{\partial \Psi}{\partial \mathbf{C}} + \mathbf{F}^{v-1}2\frac{\partial \Psi}{\partial \mathbf{C}^e}\mathbf{F}^{v-T}\right) : \frac{1}{2}\dot{\mathbf{C}} - 2\frac{\partial \Psi}{\partial \mathbf{C}^e} : \mathbf{C}^e\mathbf{L}^v + \mathbf{F}^{ne}2\frac{\partial \Psi}{\partial \mathbf{C}^{ne}}\mathbf{F}^{ne^T} : \mathbf{L}^v - 2\frac{\partial \Psi}{\partial \mathbf{C}^{ne}} : \mathbf{C}^{ne}\mathbf{L}^{ne}. \tag{13}$$

Substituting the above expression into eq. (11) for the entropy inequality gives,

$$\begin{aligned}(T - T_e)\,\dot{\eta}^c + (T - T_e)\,\frac{\nabla_{\mathbf{X}} \cdot \mathbf{Q}^c}{T_e} - \frac{1}{T}\mathbf{Q}^k \cdot \nabla_{\mathbf{X}} T - \frac{T}{T_e^2}\mathbf{Q}^c \cdot \nabla_{\mathbf{X}} T_e \\ + \left(\mathbf{S} - \left(2\frac{\partial \Psi}{\partial \mathbf{C}} + \mathbf{F}^{v-1}2\frac{\partial \Psi}{\partial \mathbf{C}^e}\mathbf{F}^{v-T}\right)\right) : \frac{1}{2}\dot{\mathbf{C}} - \left(\eta^k + \frac{\partial \Psi}{\partial T}\right)\dot{T} - \left(\eta^c + \frac{\partial \Psi}{\partial T_e}\right)\dot{T}_e \\ + \underbrace{2\left(\mathbf{C}^e\frac{\partial \Psi}{\partial \mathbf{C}^e}\right) : \mathbf{L}^v}_{W^I} \underbrace{- \mathbf{F}^{ne}2\frac{\partial \Psi}{\partial \mathbf{C}^{ne}}\mathbf{F}^{ne^T} : \mathbf{L}^v + 2\mathbf{C}^{ne}\frac{\partial \Psi}{\partial \mathbf{C}^{ne}} : \mathbf{L}^{nv}}_{W^N} \geq 0,\end{aligned} \tag{14}$$

where W^I and W^N represent the internal dissipation from local segmental motions and network deformation, respectively. Considering an arbitrary approach to equilibrium, where $\dot{T}_e$, $\dot{T}$ and $\dot{C}$ vary independently, we arrive at the following definitions for the second Piola-Kirchhoff stress tensor and entropy densities,

$$\mathbf{S} = 2\frac{\partial \Psi}{\partial \mathbf{C}} + \mathbf{F}^{v-1}2\frac{\partial \Psi}{\partial \mathbf{C}^e}\mathbf{F}^{v-T}, \quad \eta^k = -\frac{\partial \Psi}{\partial T}, \quad \eta^c = -\frac{\partial \Psi}{\partial T_e}. \tag{15}$$

The Cauchy stress can be evaluated from $\mathbf{S}$ as, $\boldsymbol{\sigma} = J^{-1}\mathbf{F}\mathbf{S}\mathbf{F}^T = J^{-1}\left(2\mathbf{F}\frac{\partial \Psi}{\partial \mathbf{C}}\mathbf{F}^T + \mathbf{F}^e 2\frac{\partial \Psi}{\partial \mathbf{C}^e}\mathbf{F}^{e^T}\right)$.

To develop constitutive relations for the remaining internal variables, eqs. (15) and (13) are applied to simplify the first law in eq. (10),

$$\dot{e^k} + \dot{e^c} = 2\frac{\partial \Psi}{\partial \mathbf{C}} : \frac{1}{2}\dot{\mathbf{C}} + 2\frac{\partial \Psi}{\partial \mathbf{C}^e} : \frac{1}{2}\dot{\mathbf{C}}^e + 2\frac{\partial \Psi}{\partial \mathbf{C}^{ne}} : \frac{1}{2}\dot{\mathbf{C}}^{ne} + W^{I,k} + W^{I,c} + W^N - \nabla_{\mathbf{X}} \cdot \mathbf{Q}^k - \nabla_{\mathbf{X}} \cdot \mathbf{Q}^c, \tag{16}$$

where the additive split of the internal dissipation from segmental rearrangements, $W^I = W^{I,k} + W^{I,c}$, follows from the split of the free energy density into kinetic and configurational contributions in eq. (7). The dissipation from network deformation can also be split into kinetic and configurational contributions. As shown in Appendix A the hardening stress response is insensitive to the split in W^N between the two material subsystems. Thus, we chose to assign the network dissipation to the kinetic subsystem to simplify the formulation.

A fundamental assumption of the effective temperature theory is that the kinetic and configurational subsystems are only weakly coupled by an internal heat transfer. Consequently the first law in eq. (16) can be decomposed into energy balances for each subsystem as [48],

$$\begin{aligned}
\dot{e}^k &= -\nabla_{\mathbf{X}} \cdot \mathbf{Q}^k - Q^{kc} + \underbrace{W^{I,k} + W^N}_{\text{dissipation}} + \underbrace{2\frac{\partial \Psi^k}{\partial \mathbf{C}} : \frac{1}{2}\dot{\mathbf{C}} + 2\frac{\partial \Psi^k}{\partial \mathbf{C}^e} : \frac{1}{2}\dot{\mathbf{C}}^e + 2\frac{\partial \Psi^k}{\partial \mathbf{C}^{ne}} : \frac{1}{2}\dot{\mathbf{C}}^{ne}}_{\text{Elastic Power}, \dot{\Psi}^k_m}, \\
\dot{e}^c &= -\nabla_{\mathbf{X}} \cdot \mathbf{Q}^c + Q^{kc} + \underbrace{W^{I,c}}_{\text{Dissipation}} + \underbrace{2\frac{\partial \Psi^c}{\partial \mathbf{C}} : \frac{1}{2}\dot{\mathbf{C}} + 2\frac{\partial \Psi^c}{\partial \mathbf{C}^e} : \frac{1}{2}\dot{\mathbf{C}}^e + 2\frac{\partial \Psi^c}{\partial \mathbf{C}^{ne}} : \frac{1}{2}\dot{\mathbf{C}}^{ne}}_{\text{Elastic Power}, \dot{\Psi}^c_m},
\end{aligned} \tag{17}$$

where Q^{kc} is the heat transfer between the kinetic and configurational subsystems. .We can further apply the decomposition of Helmholtz free energy density eq. (7) and its expansion eq. (13) to simplify above equations,

$$\begin{aligned}
T\dot{\eta}^k &= -\nabla_{\mathbf{X}} \cdot \mathbf{Q}^k - Q^{kc} + W^{I,k} + W^N, \\
T_e\dot{\eta}^c &= -\nabla_{\mathbf{X}} \cdot \mathbf{Q}^c + Q^{kc} + W^{I,c},
\end{aligned} \tag{18}$$

The above equations can be applied to eliminate the configurational heat flux in the second law eq. (14) to give the reduced dissipation inequality:

$$\begin{aligned}
-(T_e - T)\frac{Q^{kc}}{T_e} - \frac{1}{T}\mathbf{Q}^k \cdot \nabla_{\mathbf{X}} T - \frac{T}{T_e^2}\mathbf{Q}^c \cdot \nabla_{\mathbf{X}} T_e + \\
\left(2\mathbf{C}^e \frac{\partial \Psi^k}{\partial \mathbf{C}^e} + 2\frac{T}{T_e}\mathbf{C}^e \frac{\partial \Psi^c}{\partial \mathbf{C}^e} - 2\mathbf{F}^{ne} \frac{\partial \Psi^k}{\partial \mathbf{C}^{ne}} \mathbf{F}^{ne^T}\right) : \mathbf{L}^v + 2\mathbf{C}^{ne} \frac{\partial \Psi^k}{\partial \mathbf{C}^{ne}} : \mathbf{L}^{nv} \geq 0,
\end{aligned} \tag{19}$$

The last two terms in the above equation can be rewritten as,

$$\begin{aligned}
\left(2\mathbf{C}^e \frac{\partial \Psi^k}{\partial \mathbf{C}^e} + 2\frac{T}{T_e}\mathbf{C}^e \frac{\partial \Psi^c}{\partial \mathbf{C}^e} - 2\mathbf{F}^{ne} \frac{\partial \Psi^k}{\partial \mathbf{C}^{ne}} \mathbf{F}^{ne^T}\right) : \mathbf{L}^v &= \left(\boldsymbol{\tau}^{NEQ}\mathbf{b}^{e^{-1}} - \mathbf{F}^{e^{-T}}\boldsymbol{\tau}^B\mathbf{F}^{e^{-1}}\right) : \mathbf{F}^e\mathbf{L}^v\mathbf{F}^{e^T} \\
2\mathbf{C}^{ne} \frac{\partial \Psi^k}{\partial \mathbf{C}^{ne}} : \mathbf{L}^{nv} &= \boldsymbol{\tau}^B\mathbf{b}^{ne^{-1}} : \mathbf{F}^{ne}\mathbf{L}^{nv}\mathbf{F}^{ne^T},
\end{aligned} \tag{20}$$

where the Kirchhoff nonequilibrium (flow) stress $\boldsymbol{\tau}^{NEQ}$ and backstress $\boldsymbol{\tau}^B$ are given by.

$$\begin{aligned}
\boldsymbol{\tau}^{NEQ} &= 2\mathbf{F}^e \left(\frac{\partial \Psi^k}{\partial \mathbf{C}^e} + \frac{T}{T_e}\frac{\partial \Psi^c}{\partial \mathbf{C}^e}\right)\mathbf{F}^{e^T}, \\
\boldsymbol{\tau}^B &= 2\mathbf{F}^{ne} \frac{\partial \Psi^k}{\partial \mathbf{C}^{ne}} \mathbf{F}^{ne^T}.
\end{aligned} \tag{21}$$

We now assume that the material is initially isotropic, such that Ψ is an isotropic tensor function that can be equivalently expressed in terms of $\Psi(T, T_e, \mathbf{b}, \mathbf{b}^e, \mathbf{b}^{ne})$. Then $\boldsymbol{\tau}^{NEQ}$ is coaxial with $\mathbf{b}^e$ and $\boldsymbol{\tau}^B$ is coaxial with $\mathbf{b}^{ne}$, which causes $\boldsymbol{\tau}^{NEQ}\mathbf{b}^{e^{-1}}$ and $\boldsymbol{\tau}^B\mathbf{b}^{ne^{-1}}$ to be symmetric. Furthermore, we showed in Sec. 2.2.1 that the constitutive assumptions for the viscous rotations resulted in $\mathbf{F}^e = \mathbf{V}^e$ and $\mathbf{F}^{ne} = \mathbf{V}^{ne}$ being symmetric and coaxial with each other. As a result $\mathbf{F}^e = \sqrt{\mathbf{b}^e}$ is coaxial with $\boldsymbol{\tau}^N$ and $\mathbf{F}^{e^{-T}}\boldsymbol{\tau}^B\mathbf{F}^{e^{-1}} = \boldsymbol{\tau}^B\mathbf{b}^{e^{-1}}$ and symmetric. The rate of viscous deformation $\mathbf{F}^e\mathbf{L}^v\mathbf{F}^{e^T}$ can

be expanded into symmetric and skew parts, where the symmetric part is the Lie derivative of the elastic left deformation tensor, sym $\left[\mathbf{F}^e\mathbf{L}^v\mathbf{F}^{e^T}\right] = -\frac{1}{2}\mathbf{F}\dot{\mathbf{C}^{v^{-1}}}\mathbf{F}^T = -\frac{1}{2}\mathscr{L}_v\mathbf{b}^e$. Likewise, sym $\left[\mathbf{F}^{ne}\mathbf{L}^{nv}\mathbf{F}^{ne^T}\right] = -\frac{1}{2}\mathbf{F}^v\dot{\mathbf{C}^{nv^{-1}}}\mathbf{F}^{v^T} = -\frac{1}{2}\mathscr{L}_v\mathbf{b}^{ne}$. With these results, we can rewrite the reduced dissipation inequality in eq. (19) as,

$$-\left(T_e - T\right)\frac{Q^{kc}}{T_e} - \frac{1}{T}\mathbf{Q}^k\cdot\nabla_{\mathbf{X}}T - \frac{T}{T_e^2}\mathbf{Q}^c\cdot\nabla_{\mathbf{X}}T_e - \left(\boldsymbol{\tau}^{NEQ} - \boldsymbol{\tau}^B\right) : \frac{1}{2}\mathscr{L}_v\mathbf{b}^e\mathbf{b}^{e^{-1}} - \boldsymbol{\tau}^B : \frac{1}{2}\mathscr{L}_v\mathbf{b}^{ne}\mathbf{b}^{ne^{-1}} \geq 0. \tag{22}$$

The backstress $\boldsymbol{\tau}^B$ is coaxial with $\boldsymbol{\tau}^{NEQ}$ because $\mathbf{b}^e$ is coaxial with $\mathbf{b}^{ne}$.

To satisfy the positive dissipation criteria, each term of eq. (22) must be positive. Positive thermal dissipation can be satisfied by specifying a Fourier-type linear conduction law for heat transfer in the kinetic and configurational subsystems and for the inter-subsystem heat transfer

$$\mathbf{q}^k = -k^k\nabla_{\mathbf{X}}T, \quad \mathbf{q}^c = -k^c\nabla_{\mathbf{X}}T_e, \quad Q^{kc} = -K\left(T_e - T\right), \tag{23}$$

where $\mathbf{q}^k = 1/\det(\mathbf{F})\mathbf{F}\mathbf{Q}^k$ and $\mathbf{q}^c = 1/\det(\mathbf{F})\mathbf{F}\mathbf{Q}^c$ are the spatial heat fluxes of the kinetic and configurational subsystems, $k^k \geq 0$ and $k^c \geq 0$ are the thermal conductivity of each subsystem, and $K > 0$ is the inter-subsystem thermal conductivity. To satisfy the positive dissipation criteria for the viscous dissipation, we assumed the following linear relationships,

$$\begin{aligned} -\frac{1}{2}\mathscr{L}_v\mathbf{b}^e\mathbf{b}^{e^{-1}} &= \frac{1}{2\nu^I}\boldsymbol{\zeta}, \quad \boldsymbol{\zeta} = \boldsymbol{\tau}^{NEQ} - \boldsymbol{\tau}^B \\ -\frac{1}{2}\mathscr{L}_v\mathbf{b}^{ne}\mathbf{b}^{ne^{-1}} &= \frac{1}{2\nu^N}\boldsymbol{\tau}^B, \end{aligned} \tag{24}$$

where $\nu^I > 0$ and $\nu^N > 0$ are the viscous resistances to local segmental rearrangements and network deformation respectively.

We can obtain the evolution equations for T and T_e by substituting the constitutive relations in eq. (15) for the entropy densities and eq. (23) for the heat conduction into the energy balance for the kinetic and configurational susbystems eq. (18) and rearranging terms,

$$\begin{aligned} c_g\dot{T} = K\left(T_e - T\right) - \left(2\mathbf{F}^e\frac{\partial\Psi^k}{\partial\mathbf{C}^e}\mathbf{F}^{e^T} - \boldsymbol{\tau}^B\right) : \frac{1}{2}\mathscr{L}_v\mathbf{b}^e\mathbf{b}^{e^{-1}} - \boldsymbol{\tau}^B : \frac{1}{2}\mathscr{L}_v\mathbf{b}^{ne}\mathbf{b}^{ne^{-1}} \\ - 2T\frac{\partial\eta^k}{\partial\mathbf{C}} : \frac{1}{2}\dot{\mathbf{C}} + T\mathbf{C}^e\frac{\partial\eta^k}{\partial\mathbf{C}^e} : \mathbf{D}^v + k^k\nabla_{\mathbf{X}}\cdot\left(\mathbf{C}^{-1}\nabla_{\mathbf{X}}T\right), \end{aligned} \tag{25}$$

$$\Delta c\dot{T}_e = -K\left(T_e - T\right) - \mathbf{F}^e\frac{\partial\Psi^c}{\partial\mathbf{C}^e}\mathbf{F}^{e^T} : \frac{1}{2}\mathscr{L}_v\mathbf{b}^e\mathbf{b}^{e^{-1}} - 2T_e\frac{\partial\eta^c}{\partial\mathbf{C}} : \frac{1}{2}\dot{\mathbf{C}} + T_e\mathbf{C}^e\frac{\partial\eta^c}{\partial\mathbf{C}^e} : \mathbf{D}^v + k^c\nabla_{\mathbf{X}}\cdot\left(\mathbf{C}^{-1}\nabla_{\mathbf{X}}T_e\right), \tag{26}$$

where $c_g = -T\frac{\partial^2\Psi^k}{\partial T^2}$ is the heat capacity of the kinetic subsystem and $\Delta c = -T_e\frac{\partial^2\Psi^c}{\partial T_e^2}$ is the heat capacity of the configurational subsystem. Dividing the governing equation for T_e by Δc and defining the structural relaxation times as $\tau_R = \frac{K}{\Delta c}$ gives the familiar expression for the evolution of the effective temperature,

$$\dot{T}_e = -\frac{1}{\tau_R}\left(T_e - T\right) - \frac{1}{\Delta c}\mathbf{F}^e\frac{\partial\Psi^c}{\partial\mathbf{C}^e}\mathbf{F}^{e^T} : \frac{1}{2}\mathscr{L}_v\mathbf{b}^e\mathbf{b}^{e^{-1}} - \frac{2T_e}{\Delta c}\frac{\partial\eta^c}{\partial\mathbf{C}} : \frac{1}{2}\dot{\mathbf{C}} + \frac{T_e}{\Delta c}\mathbf{C}^e\frac{\partial\eta^c}{\partial\mathbf{C}^e} : \mathbf{D}^v + \frac{k^c}{\Delta c}\nabla_{\mathbf{X}}\cdot\left(\mathbf{C}^{-1}\nabla_{\mathbf{X}}T_e\right). \tag{27}$$

Equation (27) is identical to the evolution equation for T_e in the Xiao and Nguyen model [19] because of the assumption that the stored energy of network deformation is part of the kinetic subsystem and not the configurational subsystem. The consequences of this assumption are discussed in Appendix A. Xiao and Nguyen [19] discussed the physical significance of eq. (27) in detail. The first term on the right hand side describes structural relaxation which drives the configurational subsystems equilibrium. Conversely, the second term represents the mechanical rejuvenation that drives configurational subsystems away from equilibrium. The third and fourth term are thermomechanical coupling terms while the last term represents the diffusion of the effective temperatures.

2.2.3. Incorporating a relaxation spectrum

Amorphous polymers typically exhibit a broad stress and structural relaxation spectrums, which must be represented to accurately capture the kinetics of physical aging, post-yield softening response, and temperature dependence of the stress response for temperatures near the glass transition. Xiao and Nguyen [19] incorporated a discrete spectrum of stress relaxation processes into the effective temperature theory by applying parallel multiplicative decompositions of deformation gradient into elastic and viscous parts,

$$\mathbf{F} = \mathbf{F}^{\mathrm{e}}_j \mathbf{F}^{\mathrm{v}}_j, \quad j = 1..N \tag{28}$$

To incorporate kinematic hardening from network deformation and relaxation, we assume that the viscous deformation of each process can be further decomposed into elastic and viscous network components,

$$\mathbf{F}^v_j = \mathbf{F}^{\mathrm{ne}}_j \mathbf{F}^{\mathrm{nv}}_j, \quad j = 1..N. \tag{29}$$

This decouples the kinematics of network deformation and relaxation of each process, which significantly simplifies the theoretical developments. We apply the same constitutive assumption assigning all of the rotation to the viscous deformations for each process $\mathbf{R}^{nv}_k = \mathbf{R}^v_k = \mathbf{R}$, such that $\mathbf{F}^e_k$ and $\mathbf{F}^{ne}_k$ are symmetric and coaxial with each other.

Following Xiao and Nguyen [19], we assume a discrete distribution of configurational subsystems and their associated effective temperatures T_{e_i} for $i = 1..P$ to incorporate a spectrum of structural relaxation times. Then the Helmholtz free energy density can be decomposed additively into the respective contributions from the kinetic and configurational subsystems as,

$$\Psi = \Psi^k + \sum_i^P \Psi^c_i = \left(e^k - T\eta^k\right) + \sum_i^P \left(e^c_i - T_{e_i}\eta^c_i\right) \tag{30}$$

For simplicity, we assume that the configurational subsystems do not interact with each other, and they only interact with the kinetic subsystem through a inter-subsystem heat transfer. This results in the following decomposition of the first law into energy balances for each subsystem,

$$\begin{aligned} \dot{e}^k &= -\nabla_{\mathbf{X}} \cdot \mathbf{Q}^k - \sum_i^P Q^{kc}_i + W^{I,k} + W^N + \dot{\Psi}^k_m \\ \dot{e}^c_i &= -\nabla_{\mathbf{X}} \cdot \mathbf{Q}^c_i + Q^{kc} + W^{I,c} + \dot{\Psi}^c_m, \end{aligned} \tag{31}$$

where Q^{kc}_i is the heat transfer between the kinetic subsystem and the configurational subsystem i. The thermodynamic interactions between each subsystems and contributions to the internal energy are illustrated in Fig. 3.

Applying these assumptions to effective temperature thermodynamic theory in Sec. 2.2.2, we can arrive at the following definitions for the stress and entropy densities,

$$\mathbf{S} = 2\frac{\partial \Psi}{\partial \mathbf{C}} + \sum_j^N \mathbf{F}^{v-1}_j 2\frac{\partial \Psi}{\partial \mathbf{C}^e_j} \mathbf{F}^{v-T}_j, \quad \eta^k = -\frac{\partial \Psi}{\partial T}, \quad \eta^c_i = -\frac{\partial \Psi}{\partial T_{e_i}}, \tag{32}$$

and obtain the following reduced dissipation inequality ,

$$-\sum_i^P \left(T_{e_i} - T\right)\frac{Q^{kc}_i}{T_{e_i}} - \frac{1}{T}\mathbf{Q}^k \cdot \nabla_{\mathbf{X}} T - \sum_i^P \frac{T}{T^2_{e_i}} \mathbf{Q}^c_i \cdot \nabla_{\mathbf{X}} T_{e_i} - \sum_j^N \left(\boldsymbol{\tau}^{NEQ}_j - \boldsymbol{\tau}^B_j\right) : \frac{1}{2}\mathscr{L}_v \mathbf{b}^e_j \mathbf{b}^{e^{-1}}_j - \sum_j^N \boldsymbol{\tau}^B_j : \frac{1}{2}\mathscr{L}_v \mathbf{b}^{ne}_j \mathbf{b}^{ne^{-1}}_j \geq 0. \tag{33}$$

The Kirchhoff nonequilibrium stresses and backstresses for stress relaxation processes are defined as,

$$\boldsymbol{\tau}^{NEQ}_j = 2\mathbf{F}^e_j \frac{\partial \Psi^k}{\partial \mathbf{C}^e_j} \mathbf{F}^{e^T}_j + \sum_i^P 2\frac{T}{T_{e_i}} \mathbf{F}^e_j \frac{\partial \Psi^c_i}{\partial \mathbf{C}^e_j} \mathbf{F}^{e^T}_j, \quad \boldsymbol{\tau}^B_j = 2\mathbf{F}^{ne}_j \frac{\partial \Psi^k}{\partial \mathbf{C}^{ne}_j} \mathbf{F}^{ne^T}_j, \quad \text{for } j = 1..N. \tag{34}$$

To satisfy the second law for an arbitrary thermal and deformation history, we can define the following Fourier-type heat conduction laws

$$\mathbf{q}^k = -k^k \nabla_{\mathbf{x}} T, \quad \mathbf{q}^c_i = -k^c_i \nabla_{\mathbf{x}} T_{e_i}, \quad Q^{kc}_i = -K_i\left(T_{e_i} - T\right), \tag{35}$$

and evolution equations for the viscous deformations

$$
\begin{aligned}
-\frac{1}{2}\mathscr{L}_v \mathbf{b}_j^e \mathbf{b}_j^{e^{-1}} &= \frac{1}{2\nu_j^I}\boldsymbol{\zeta}_j, \quad \boldsymbol{\zeta}_j = \boldsymbol{\tau}_j^{NEQ} - \boldsymbol{\tau}^B{}_j \\
-\frac{1}{2}\mathscr{L}_v \mathbf{b}_j^{ne} \mathbf{b}_j^{ne^{-1}} &= \frac{1}{2\nu_j^N}\boldsymbol{\tau}_j^B.
\end{aligned}
\tag{36}
$$

Substituting the constitutive relations into the energy balances in eq. (31) gives the following evolution equations for the temperature and effective temperatures,

$$
\begin{aligned}
c_g \dot{T} = \sum_i^P K_i (T_{e_i} - T) - \sum_j^N \left(2\mathbf{F}_j^e \frac{\partial \Psi^k}{\partial \mathbf{C}_j^e} \mathbf{F}_j^{e^T} - \boldsymbol{\tau}_j^B \right) : \frac{1}{2}\mathscr{L}_v \mathbf{b}_j^e \mathbf{b}_j^{e^{-1}} - \sum_j^N \boldsymbol{\tau}_j^B : \frac{1}{2}\mathscr{L}_v \mathbf{b}_j^{ne} \mathbf{b}_j^{ne^{-1}} \\
- 2T \frac{\partial \eta^k}{\partial \mathbf{C}} : \frac{1}{2}\dot{\mathbf{C}} + \sum_j^N T \mathbf{C}_j^e \frac{\partial \eta^k}{\partial \mathbf{C}_j^e} : \mathbf{D}_j^{\mathrm{v}} + k^k \nabla_{\mathbf{X}} \cdot \left(\mathbf{C}^{-1} \nabla_{\mathbf{X}} T \right),
\end{aligned}
\tag{37}
$$

$$
\begin{aligned}
\dot{T}_{e_i} = -\frac{1}{\tau_{R_i}} (T_{e_i} - T) - \sum_j^N \frac{2}{\Delta c_i} \mathbf{F}_j^e \frac{\partial \Psi^c}{\partial \mathbf{C}_j^e} \mathbf{F}_j^{e^T} : \frac{1}{2}\mathscr{L}_v \mathbf{b}_j^e \mathbf{b}_j^{e^{-1}} - 2\frac{T_{e_i}}{\Delta c_i} \frac{\partial \eta_i^c}{\partial \mathbf{C}} : \frac{1}{2}\dot{\mathbf{C}} \\
+ \sum_j^N \frac{T_{e_i}}{\Delta c_i} \mathbf{C}_j^e \frac{\partial \eta_i^c}{\partial \mathbf{C}_j^e} : \mathbf{D}_j^{\mathrm{v}} + \frac{k_i^c}{\Delta c_i} \nabla_{\mathbf{X}} \cdot \left(\mathbf{C}^{-1} \nabla_{\mathbf{X}} T_e \right),
\end{aligned}
\tag{38}
$$

where $c_g = -T\frac{\partial^2 \Psi^k}{\partial T^2}$ is the heat capacity of the kinetic subsystem, $\Delta c_i = -T_{e_i}\frac{\partial^2 \Psi^c}{\partial T_{e_i}^2}$ is the heat capacity and $\tau_{R_i} = \frac{K_i}{\Delta c_i}$ is the structural relaxation time of the subsystem i,

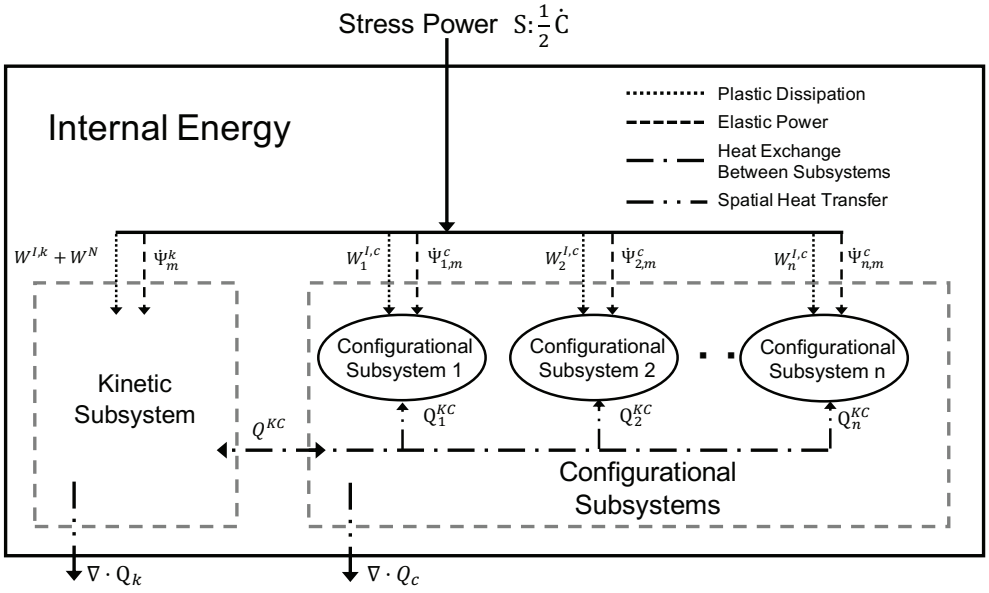

Figure 3: Diagram of the energy transfer between the kinetic and configurational subsystems and contributions to the internal energy. The diagram shows the contribution of the stress power and spatial heat transfer to the total internal energy, as well as the configurational heat transfer between the subsystems. The term $W^{I,k}$ and $W_i^{I,c}$ are the internal dissipation rates from local segmental motions in the kinetic subsystem and i^{th} configurational subsystem, W^N is the dissipation rate from network deformation, $\dot{\Psi}_m^k$ and $\dot{\Psi}_{i,m}^c$ are the elastic power flowing into the kinetic subsystem and i^{th} configurational subsystem.

2.2.4. Constitutive model for Polycarbonate

In the following subsection, we apply the multiprocess effective temperature theory in Sec. 2.2.3 to develop a constitutive model for polycarbonate, which is a common amorphous thermoplastic. For the free energy density in eq. (30), the compressible Neo-Hookean model is applied to describe the internal energy and entropy densities associated with local segmental motion in the kinetic and configurational subsystems,

$$\begin{aligned}\Psi^k &= \sum_j^P \frac{(1-a)\mu_j^{neq}}{2}\left(\mathrm{tr}\left(\bar{\mathbf{C}}_j^e\right)-3\right)+\frac{\kappa}{4}\left(J^2-2\log J-1\right)+c_{g_0}\left(T-T_0-T\ln\frac{T}{T_0}\right)-\frac{c_{g_1}}{2}(T-T_0)^2+\sum_j^P \xi\left(\bar{\mathbf{C}}_j^{ne}\right),\\ \Psi_i^c &= \sum_j^P \frac{a_i\mu_j^{neq}}{2}\left(\mathrm{tr}\left(\bar{\mathbf{C}}_j^e\right)-3\right)+\Delta c_{0_i}\left(T_{e_i}-T_0-T_{e_i}\ln\frac{T_{e_i}}{T_2}\right)-\frac{\Delta c_{1_i}}{2}\left(T_{e_i}-T_2\right)^2,\end{aligned} \tag{39}$$

The Arruda-Boyce eight-chain model [28] is applied to describe the internal energy associated with network deformation to account for the limiting stretch of the network structure:

$$\xi\left(\bar{\mathbf{C}}_j^{ne}\right)=\mu_j^{back}\lambda_L^2\left[\frac{\bar{\lambda}_{eff_j}}{\lambda_L}x_j+\ln\frac{x_j}{\sinh x_j}\right],\quad \bar{\lambda}_{eff_j}=\sqrt{\frac{1}{3}\mathrm{tr}\bar{\mathbf{C}}_j^{ne}},\quad x_j=\mathscr{L}^{-1}\left(\frac{\bar{\lambda}_{eff_j}}{\lambda_L}\right) \tag{40}$$

where $J=\det\mathbf{F}$ is the volumetric deformation, $J_j^e=\det\mathbf{F}_j^e$ is the elastic part of J and $J_j^{N,e}=\det\mathbf{F}_j^{N,e}$ is the elastic network volumetric deformation. The $\bar{\mathbf{C}}_j^e=J_j^{e^{-2/3}}\mathbf{C}_j^e$ and $\bar{\mathbf{C}}_j^{ne}=J_j^{e^{-2/3}}\mathbf{C}_j^{ne}$ are the isochoric parts of the elastic and elastic network right deformation tensors respectively. The parameter κ is the bulk modulus, T_2 is the Kauzmann temperature, λ_L is the limiting stretch in the eight-chain model. The μ_j^{neq} for $j=1..N$ forms the spectrum of non-equilibrium shear moduli for the stored energy of local segmental rearrangements and the μ_j^{back} describes the spectrum of shear moduli for the stored energy of network deformation. The parameters c_{g_0} and c_{g_1} are the coefficients of the heat capacity of the kinetic subsystem, where $c_g=c_{g0}+c_{g1}T$; Δc_{0_i} and Δc_{1_i} are the coefficients of the heat capacity of the configurational subsystems, where $\Delta c_i=\Delta c_{0_i}+\Delta c_{1_i}T_{e_i}$. We split the inelastic internal energy into contributions for the kinetic and configurational subsystems using a fractional parameter $0\leq a\leq 1$, where $\sum_i^P a_i=a$ is the total configurational contributions to the internal inelastic energy, and $1-a$ is the kinetic contribution. For simplicity, we assume that the physical properties share the same distribution function over the P configurational subsystems. Thus we can write the properties as, $\mu_i{}^{eq}=\phi_i\mu^{eq}$, $a_i=\phi_i a$, $\Delta c_{0_i}=\phi_i\Delta c_0$, $\Delta c_{1_i}=\phi_i\Delta c_1$, where $0<\phi_i<1$ and $\sum_i^P\phi_i=1$. The Δc_0 and Δc_1 represent the difference between the rubbery and glassy heat capacity, $c_r=(c_{g0}+\Delta c_0)+(c_{g1}+\Delta c_1)T$. Note for thermosets, the configurational Ψ can be augmented with an entropic rubber elasticity model to describe the high temperature elastic response [19].

The second Piola-Kirchhoff stress can be evaluated as defined in eq. (32) and the Cauchy stress can be evaluated as $\sigma=\frac{1}{J}\mathbf{F}\mathbf{S}\mathbf{F}^T$,

$$\sigma=\frac{1}{J}\sum_j^P\underbrace{\mu_j^{neq}\left(\bar{\mathbf{b}}_j^{ne}-\frac{1}{3}\mathrm{tr}\left(\bar{\mathbf{b}}_j^e\right)\mathbf{I}\right)}_{\sigma_j^{neq}}+\underbrace{\frac{1}{2J}\kappa\left(J^2-1\right)}_{p}\mathbf{I}, \tag{41}$$

where $\mathbf{I}$ is the second-order identity tensor, $\bar{\mathbf{b}}_j^e=J_j^{e^{-2/3}}\mathbf{b}_j^e$ and $\bar{\mathbf{b}}_j^{ne}=J_j^{e^{-2/3}}\mathbf{b}_j^{ne}$. The Kirchhoff nonequilibrium flow stress and backstress can be evaluated as,

$$\begin{aligned}\boldsymbol{\tau}_j^{NEQ}&=\textstyle\sum_i^P\phi_i\left(1+a\left(\frac{T}{T_{e_i}}-1\right)\right)\mu_j^{neq}\left(\bar{\mathbf{b}}_j^e-\frac{1}{3}\mathrm{tr}\left(\bar{\mathbf{b}}_j^e\right)\mathbf{I}\right)\\ \boldsymbol{\tau}_j^B&=\mu_j^{back}\frac{\lambda_L}{\bar{\lambda}_{eff_j}}\mathscr{L}^{-1}\left(\frac{\bar{\lambda}_{eff_j}}{\lambda_L}\right)\left(\bar{\mathbf{b}}_j^{ne}-\frac{1}{3}\mathrm{tr}\left(\bar{\mathbf{b}}_j^{ne}\right)\mathbf{I}\right),\end{aligned} \tag{42}$$

From eq. (24), the inelastic rate of deformation tensor is related to the flow stress $\boldsymbol{\zeta}_j=\boldsymbol{\tau}_j^{NEQ}-\boldsymbol{\tau}_j^B$ through the viscous resistance to local segmental rearrangements ν_j^I while the rate of deformation tensor for network relaxation is related to

the backstress $\boldsymbol{\tau}_j^B$ through the viscous resistance to network deformation ν_j^N. We applied the model proposed by Xiao and Nguyen [19] for ν_j^I that used the Adam-Gibbs model [22] and the Eyring model [8] to describe the temperature and deformation dependence of viscosity:

$$-\frac{1}{2}\mathscr{L}_v\mathbf{b}_j^e\mathbf{b}_j^{e^{-1}} = \frac{1}{2\nu_j^I}\boldsymbol{\zeta}_j, \quad \nu_j^I = \nu_j^{I,ref}\exp\left(\frac{B}{T\eta^c}\right)\frac{V_Z Z}{RT}\left[\sinh(\frac{V_Z Z}{RT})\right]^{-1}. \tag{43}$$

The $\eta^c = \sum_i^P \eta_i^c$ is the aggregate configurational entropy of the subsystem, $\boldsymbol{\zeta} = \sum_j^N \boldsymbol{\zeta}_i$ is the total driving stress, $Z = \sqrt{\frac{1}{2}\boldsymbol{\zeta}:\boldsymbol{\zeta}}$ is the magnitude of the driving stress, B is the thermal activation energy, and V_Z is the activation volume for local segmental rearrangements.

The Eyring model was applied to describe the temperature-dependence and strain rate-dependence of the viscous resistance to network deformation:

$$-\frac{1}{2}\mathscr{L}_v\mathbf{b}_j^{ne}\mathbf{b}_j^{ne^{-1}} = \frac{1}{2\nu^N{}_j}\boldsymbol{\tau}_j^B, \quad \nu_j^N = \nu_j^{N,ref}\exp\left(\frac{A}{T}\right)\left(\frac{\alpha_0-\alpha_c}{\alpha-\alpha_c}\alpha^{-m}\right)\frac{V_S S^B}{RT}\left[\sinh\frac{V_S S^B}{RT}\right]^{-1}, \tag{44}$$

where $\boldsymbol{\tau}^B = \sum_j^N \boldsymbol{\tau}_j^B$ is the total backstress, $S^B = \sqrt{\frac{1}{2}\boldsymbol{\tau}^B:\boldsymbol{\tau}^B}$ is the magnitude of the total back stress, A is the thermal activation parameter, and V_S is the activation volume for network relaxation. Various studies have proposed a dependence of ν_j^N on the network deformation, e.g., $\mathbf{b}^{ne}$, to capture the dramatic hardening at large strains [40, 44, 51]. Dupaix et. al. [39] showed that specifying a dependence on the network orientation parameter α of the 8-chain network model produced a more accurate dependence of the stress response on the strain state, i.e. uniaxial tension vs. plane strain. The orientation parameter is defined as, $\alpha = \pi/2 - \max\{\alpha_1,\alpha_2,\alpha_3\}$, where $(\alpha_1,\alpha_2,\alpha_3)$ are the angles between the end-to-end vector of a polymer chain of the 8-chain network model and each of the three principal axes. The polymer chains rotate and stretch to align in the direction of deformation and α describes the extent of chain alignment with a principle axis. The parameter m is a power-law exponent for α and $\alpha_0 = 0.616$ rad for a unit cube in the eight-chain model. The parameter α_c is the orientation level where the relaxation cutoff occurs, which was introduced to avoid underestimating strain hardening at very large strains [39]. Dupaix et. al. [39] showed that the uniaxial tension and plane strain hardening stress response reached the limiting stretch at the same value of α. Note that the ν_j^N does not depend on the configurational entropy η or the effective temperatures T_i^e. Appendix A compares the effects on the hardening stress response of applying the Arrhenius model versus the Adam-Gibbs model, which imposes a dependence on η^c as well as T. The Adam-Gibbs model resulted in a decrease in the hardening modulus with increasing strain rate, which is opposite of what is observed in experiments for polycarbonate.

For the applications in this model, we will neglect the effects of the diffusion of T_{e_i} in eq. (27) to simplify the numerical implementation and evaluation. For the free energy density shown in eq. (39), the evolution equation for effective temperatures eq. (27) reduces to,

$$\begin{aligned}
\dot{T}_i^e &= -\frac{1}{\tau_{R_i}}(T_{e_i}-T) + \frac{a}{\Delta c_0 + \Delta c_1 T_{e_i}}\sum_i^P \frac{1}{2\tau_{S_j}}\left(\bar{\mathbf{b}}_j^e - \frac{1}{3}\mathrm{tr}\left(\bar{\mathbf{b}}_j^e\right)\mathbf{I}\right):\boldsymbol{\zeta}_j \\
\tau_{R_i} &= \tau_{R_i}^{ref}\exp\left(\frac{B}{T\eta^c}\right), \quad \tau_{S_j} = \frac{\nu_j^{I,ref}}{\mu_j^{neq}}\exp\left(\frac{B}{T\eta^c}\right)\frac{V_Z Z}{RT}\left[\sinh(\frac{V_Z Z}{RT})\right]^{-1}
\end{aligned} \tag{45}$$

where we have substituted the evolution equation (43) for the Lie derivate $\mathbf{b}^e$. We applied the Adam-Gibbs model [22] to describe the temperature dependence and structure dependence of the structural relaxation time. In previous work, we showed that these assumptions provided accurate predictions of the effects of physical aging and mechanical rejuvenation on the stress response and the temperature-dependent enthalpy change. The proposed constitutive model was summarized in Table 1.

Kinematics

$$\mathbf{F} = \mathbf{F}^e\mathbf{F}^v, \quad \mathbf{F}^v = \mathbf{F}^{ne}\mathbf{F}^{nv}$$

Free Energy Density

$$\Psi = \Psi^k + \Psi^c$$

$$\Psi^k = \sum_j^P \frac{(1-a)\mu_j^{neq}}{2}\left(\mathrm{tr}\left(\bar{\mathbf{C}}_j^e\right) - 3\right) + \frac{\kappa}{4}\left(J^2 - 2\ln J - 1\right) + c_{g_0}\left(T - T_0 - T\ln\frac{T}{T_0}\right) - \frac{c_{g_1}}{2}(T-T_0)^2 + \sum_j^P \xi\left(\bar{\mathbf{C}}_j^{ne}\right)$$

$$\Psi_i^c = \sum_j^P \frac{a_i\mu_j^{neq}}{2}\left(\mathrm{tr}\left(\bar{\mathbf{C}}_j^e\right) - 3\right) + \Delta c_{0_i}\left(T_{e_i} - T_0 - T_{e_i}\ln\frac{T_{e_i}}{T_2}\right) - \frac{\Delta c_{1_i}}{2}\left(T_{e_i} - T_2\right)^2$$

$$\xi\left(\bar{\mathbf{C}}_j^{ne}\right) = \mu_j^{back}\lambda_L^2\left[\frac{\bar{\lambda}_{eff_j}}{\lambda_L}x_j + \ln\frac{x_j}{\sinh x_j}\right], \quad \bar{\lambda}_{eff_j} = \sqrt{\tfrac{1}{3}\mathrm{tr}\bar{\mathbf{C}}_j^{ne}}, \quad x_j = \mathscr{L}^{-1}\left(\frac{\bar{\lambda}_{eff_j}}{\lambda_L}\right)$$

Stress Response

$$\sigma = \frac{1}{J}\sum_j^P \underbrace{\mu_j^{neq}\left(\bar{\mathbf{b}}_j^{ne} - \frac{1}{3}\mathrm{tr}\left(\bar{\mathbf{b}}_j^e\right)\mathbf{I}\right)}_{\sigma_j^{neq}} + \underbrace{\frac{1}{2J}\kappa\left(J^2-1\right)}_{p}\mathbf{I}$$

Evolution Laws

$$-\tfrac{1}{2}\mathscr{L}_v\mathbf{b}_j^e\mathbf{b}_j^{e^{-1}} = \frac{1}{2\nu_j^I}\boldsymbol{\zeta}_j, \quad \nu_j^I = \nu_j^{I,ref}\exp\left(\frac{B}{T\eta^c}\right)\frac{V_Z Z}{RT}\left[\sinh\left(\frac{V_Z Z}{RT}\right)\right]^{-1}$$

$$-\tfrac{1}{2}\mathscr{L}_v\mathbf{b}_j^{ne}\mathbf{b}_j^{ne^{-1}} = \frac{1}{2\nu^N{}_j}\boldsymbol{\tau}_j^B, \quad \nu_j^N = \nu_j^{N,ref}\exp\left(\frac{A}{T}\right)\left(\frac{\alpha_0-\alpha_c}{\alpha-\alpha_c}\alpha^{-m}\right)\frac{V_S S^B}{RT}\left[\sinh\frac{V_S S^B}{RT}\right]^{-1}$$

Governing Equations

$$\dot{T}_i^e = -\frac{1}{\tau_{R_i}}\left(T_{e_i} - T\right) + \frac{a}{\Delta c_0 + \Delta c_1 T_{e_i}}\sum_i^P \frac{1}{2\tau_{S_j}}\left(\bar{\mathbf{b}}_j^e - \tfrac{1}{3}\mathrm{tr}\left(\bar{\mathbf{b}}_j^e\right)\mathbf{I}\right) : \boldsymbol{\zeta}_j$$

$$\tau_{R_i} = \tau_{R_i}^{ref}\exp\left(\frac{B}{T\eta^c}\right), \quad \tau_{S_j} = \frac{\nu_j^{I,ref}}{\mu_j^{neq}}\exp\left(\frac{B}{T\eta^c}\right)\frac{V_Z Z}{RT}\left[\sinh\left(\frac{V_Z Z}{RT}\right)\right]^{-1}$$

Table 1: Summary of the effective temperature model incorporating kinematic hardening

2.2.5. DSC simulations

We developed a finite element model of the DSC experiments in Sec. 2.1.3 to fit the spectrum of structural relaxation times (ϕ_i, τ_{R_i}). Fig. 4 shows a schematic of an axisymmetric finite element model, with height 3.2 mm and radius 1.35 mm, of the specimen used in the DSC experiments. The geometry was discretized using 10×10 bilinear quadrilateral elements. The coupled thermomechanical problem was solved using a staggered scheme. The thermal diffusion equation (37) was solved for the temperature field, and used to solve the mechanical equilibrium equations for the displacements, stress response (eqs.(41)-(44)) and effective temperatures (eq. (45)). The displacement boundary conditions were applied to fix the horizontal displacement of the axis of symmetry, $u_x(AB) = 0$, and to fix the vertical displacement of the bottom of the specimen, $u_y(AC) = 0$. The remaining surfaces were traction free. To simulate the heat transfer to the specimen, convection boundary conditions were applied on surfaces *BD* and *DC* and *AC*. Surfaces *AC* and *BD* were assumed to be in contact with the DSC aluminum pan and lid, and the heat flux between the specimen and metal can be described by $\mathbf{q} = h_1\left(T - T_{DSC}\right)\mathbf{n}$, where $\mathbf{n}$ is the direction of the surface normal, T_{DSC} is the temperature history of DSC experiments, and $h_1 = 7500\mathrm{W}/(\mathrm{m}^2\mathrm{K})$ is the heat transfer coefficient between polymer and metal obtained from Dawson et al. [53]. Surface *CD* was assumed to be in contact with air, and the heat flux between the specimen and air was described by $\mathbf{q} = h_2\left(T - T_{DSC}\right)\mathbf{n}$, where $h_2 = 10\mathrm{W}/(\mathrm{m}^2\mathrm{K})$ is the heat transfer coefficient

for air. The macroscopic specific heat flux can be calculated from eqs. (37) and (38) as,

$$\overline{Q} = \frac{1}{\rho V}\int \left((c_{g0} + c_{g1}T)\,\dot{T} + \sum_{i}^{P} \phi_i \left(\Delta c_0 + \Delta c_1 T_{e_i}\right)\dot{T}_{e_i} + \sum_{j}^{N} \boldsymbol{\zeta}_j : \mathscr{L}_v \mathbf{b}_j^e \mathbf{b}_j^{e^{-1}} + \sum_{j}^{N} \boldsymbol{\tau}_j^B : \mathscr{L}_v \mathbf{b}_j^{ne} \mathbf{b}_j^{ne^{-1}} \right) dV, \tag{46}$$

where $\rho = 1.2\mathrm{g/cm}^3$ is the density of the polymer and V is the volume of the specimen.

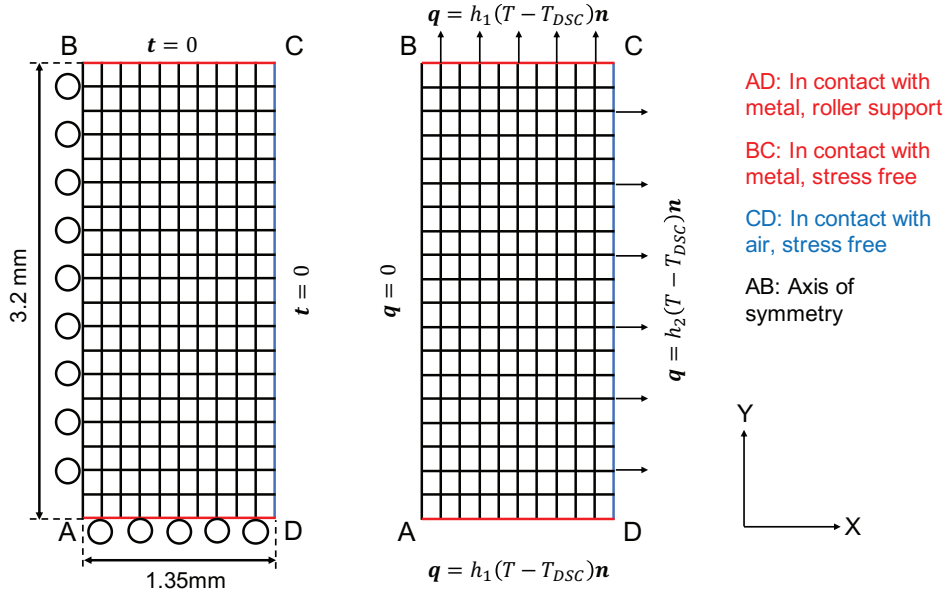

Figure 4: Finite element model of an axisymmetric cylindrical specimen.

2.2.6. *Uniaxial compression simulations*

The thermomechanical model (eqs.(41)-(45)) were applied to simulate the stress response in the uniaxial compression experiments under constant strain rate and temperature (Sec. 2.1.4). We assumed that the heat generation is negligible for the low strain rates 10^{-5} to 10^{-3} of the experiments, such that the temperature change $\dot{T}$ experienced by the specimen is negligible. We also assumed for the slow cooling rate and long annealing time of the of the experiment that specimen is under thermal equilibrium and the temperature field, effective temperature field, and stress field are homogenous. This reduced the simulations to a material point simulation for the stress response for an applied true strain rate. To calculate the initial nonequilibrium structure (T_{e_i}), the temperature was cooled from 143 °C to the test temperature at 3 °C/min and held for 30 min. The rate-dependent experiments at 37 °C were used to calibrate the model parameters for the evolution equations (43)-(44) for $\mathbf{b}^e$ and $\mathbf{b}^{ne}$, as described in Sec. 3. The model was then applied to simulate the compression test at 95 °C and load-reload tests at 27 °C without additional fitting parameters.

2.2.7. *Peel simulations*

The thermomechanical model was applied to simulate peeling of a thin polymer fiber from a rigid substrate and evaluate the effect of the post-yield stress drop and strain hardening modulus on the peel energy and intrinsic viscoplastic dissipation rate. Figure 5 shows a schematic of a plane-strain finite element model for a typical 90° peel test. The model described a polycarbonate fiber of length 20 mm and thickness 0.4 mm adhered to a rigid substrate with a pre-crack of length 7.5 mm. The fiber was discretized using a structured mesh of 337 × 14 bilinear quadrilateral elements. The surface AF was discretized using bilinear cohesive surface elements, which prescribed a traction-separation law between two initially unseparated surfaces. The displacements of the bottom surface of cohesive elements were fixed $u_X = u_Y = 0$ to simulate a rigid substrate. The remaining surfaces were assumed to be traction free. Peeling was

achieved by applying displacement u_Y at a constant speed v =0.01 mm/s at point E, which was the midpoint of the fiber thickness.

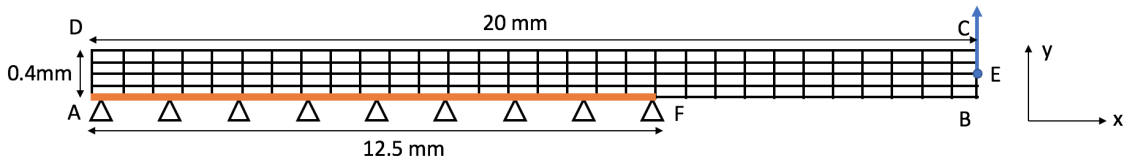

Figure 5: Finite element model of a thin fiber adhered to a rigid substate used for the simulation of 90^o peel.

The Xu-Needleman model [54] was used to describe the traction-separation constitutive relations for the cohesive surface elements. The model prescribes a potential function for the cohesive energy $\Phi(\Delta_n, \Delta_t)$ that depends on the normal separation Δ_n and tangential separation Δ_t. The normal and tangential tractions are defined as the partial derivates of the Φ relative to the normal and tangential separations, respectively. The reader is referred to work by Xu et al. [54] for a detailed derivation of the traction-separation law. The Xu-Needleman model is characterized by 5 parameters, the normal cohesive energy Φ_n, characteristic normal separation δ_n and characteristic tangential separation δ_t, ratio of tangential cohesive energy to normal cohesive energy q, normal opening after pure shear separation r. For simplicity, we set $q = 1$ and $r = 0$. We assumed $\Phi_n = 0.4\ kJ/m^2$ for the cohesive energy based on the measurements of Pitman and Ward [55] for Lexan, a commercial polycarbonate, with a similar molecular mass (Mw=17000) as the Ultimaker fiber (Mw=24000). Both the maximum normal and tangential tractions of the cohesive zone were assumed to be 50 MPa, which was approximately the draw stress exhibited in uniaxial compression stress-strain curves, after post-yield softening and before hardening, measured at 37° and strain rate $10^{-3}s^{-1}$. The maximum tractions was used to calculate characteristic separation parameters δ_n and δ_t.

The stress response of a glassy polymer at a given temperature, strain rate, and strain state can be described by 5 material properties: the Young's modulus E, Poisson's ratio ν, peak stress σ_p and draw stress σ_d under uniaxial compression, and hardening modulus H. Previous studies have shown that the ν and the ratio of the Young's modulus to the yield stress do not significantly affect the Mode I fracture energy. Here, we focused the investigation on the effects of the hardening modulus and the peak stress relative to the draw stress. A brief survey of uniaxial compression tests of different glassy polymers showed that the ratio $\frac{H}{\sigma_d}$ for uniaxial tension can vary from 0.15 to 1.21 [56, 57, 58]. Klompen et al. showed that the ratio of the peak to draw stress for uniaxial tension of PC can vary from 1.0 to 2.0 depending on the thermal history [12].

The baseline case of the parameter study is given by the model parameters in Table 2 determined for Ultimaker polycarbonate fiber. The uniaxial compression response of the baseline case at 37 °C and strain rate $10^{-3}s^{-1}$ was characterized by $\sigma_d = 50MPa$, H/σ_d =0.39, and σ_p/σ_d =1.45. The hardening modulus was calculated from the slope of true stress versus gaussian function at range of 1.4 to 1.7 (true strain 55.1 % to 67.4 %) and the draw stress was determined as the lowest stress after yield. The draw stress σ_d was maintained constant while changing either the peak stress σ_p or hardening modulus H, while keeping the other constant (Table 2) by tuning the parameters a, V_Z, and the hardening modulus scaling factor d_2 (Sec. 3). For case 1, 2, 4 and 5, the material was cooled at rate of 3 °C/min from 418K to 37 °C and annealed for 1800 s. For case 3, the material was cooled at 0.36 °C/min from 418 K to 37 °C and annealed for 2000 s.

Case	$\frac{\sigma_p}{\sigma_d}$	$\frac{H}{\sigma_d}$	V_S	a	d_2
1	1.37	0.37	103.5	0.35	0.007
2	1	0.37	180	0	0.00446
3	1.89	0.37	65.33	1	0.00573
4	1.37	0.57	102.38	0.4289	0.01
5	1.37	0.13	109.3	0.2063	0.003

Table 2: Parameter study of the effect of the post-yield stress drop and strain hardening modulus on the peel energy. The variables σ_p, σ_d and H denote the peak stress, draw stress, and hardening modulus respectively at 37 °C and strain rate of 10^{-3}/s.

The peel force was evaluated from the reaction force at node E. It can be shown, using the well-known energy balance [59, 60, 61] that the peel force is equivalent to the energy release rate for steady-state 90° peeling. For a viscoplastic material, the peel force includes the cohesive energy, the intrinsic viscoplastic dissipation rate caused by the propagation of the peel tip, the viscoplastic dissipation rate from bending the peel arm, and the stored energy of the peel arm. To derive and expression for the viscoplastic dissipation rate under constant temperature conditions, consider the balance of mechanical power of the fiber.

$$\underbrace{\int_\Omega \frac{1}{2}\mathbf{S} : \dot{\mathbf{C}} dV}_{P_{int}} = \underbrace{\int_{\partial\Omega} t \cdot v ds}_{P_{ext}} \tag{47}$$

The surface of the fiber is subjected to the cohesive traction and the peel force F, and the external power can be written as,

$$P_{ext} = F\frac{dy}{dt} - \Phi\frac{da}{dt} \tag{48}$$

where F is the peel force, dy/dt is the peel velocity and da/dt is the crack speed. The internal stress power can be written in terms of the free energy density and viscoplastic dissipation using eq. (13) as,

$$\begin{aligned} P_{int} &= \int_\Omega \mathbf{S} : \frac{1}{2}\dot{\mathbf{C}} dV \\ &= \int_\Omega \left(\dot{\Psi}_m + W^I + W^N\right) dV, \end{aligned} \tag{49}$$

where $\dot{\Psi}_m = \dot{\Psi} - \frac{\partial \Psi}{\partial T}\dot{T} - \sum_i \frac{\partial \Psi}{\partial T_{e_i}}\dot{T}_{e_i}$ is the mechanical part of the rate of the free-energy density and W^N and W^I are respectively the viscoplastic dissipation from segmental relaxation and network relaxation defined in eq. (14). The viscoplastic dissipation can be written as, $W^I = \sum_j 2\mathbf{C}^e_j \frac{\partial \Psi}{\partial \mathbf{C}^e_j} : \mathbf{L}^{\mathrm{v}}_j$ and $W^N = \sum_j \left(-\mathbf{F}^{ne}_j 2\frac{\partial \Psi}{\partial \mathbf{C}^{ne}_j}\mathbf{F}^{ne^T}_j : \mathbf{L}^v_j + 2\mathbf{C}^{ne}_j \frac{\partial \Psi}{\partial \mathbf{C}^{ne}_j} : \mathbf{L}^{nv}_j\right)$. Substituting these expressions for the internal and external power in the mechanical energy balance in eq. (47), dividing both sides by the crack speed da/dt, and assuming elongation of the peel arm is negligible such that $dy/da = 1$ at steady-state gives,

$$F = \Phi + \underbrace{\frac{1}{dy/dt}\int_\Omega \dot{\Psi}_m dV}_{\Psi'_{m,tot}} + \underbrace{\frac{1}{dy/dt}\int_\Omega W^I + W^N dV}_{D}. \tag{50}$$

The peel force F is the energy release rate for peeling that includes the cohesive energy, rate of stored mechanical energy and viscoplastic dissipation D. Plastic deformation during peeling can occur from the stress concentration at the crack tip and large bending stresses in the peel arm. The intrinsic dissipation from crack growth D^{intr} was approximated by integrating the viscoplastic dissipation rate $W^I + W^N$ in a rectangular domain bounded by the midline of the peel arm and the bottom surface of the peel arm where the cohesive tractions were non-zero. The dissipation from bending D^{bend} was approximated by integrating $W^I + W^N$ over the remaining area of the peel geometry. Bending stresses may also cause plastic deformation around the crack tip, in the domain used to evaluate D^{intr}

3. Model Parameters

Parameter	Physical significance	Values
T_{g}(K)	Glass transition temperature	383
κ (MPa)	Bulk modulus	2085.3
$V_S^I(\mathrm{cm}^3/\mathrm{mol})$	Activation volume for viscous flow	860.63
B(J/g)	Thermal activation energy	357.0
T_2(K)	Kauzmann temperature	350.428

T_0(K)	Reference temperature	416
c_{g0}(J/(gK))	Coefficient of heat capacity of kinetic subsystem	-0.3005
c_{g1}(J/(gK))	Coefficient of heat capacity of kinetic subsystem	0.003665
Δc_0(J/(gK))	Coefficient of excess heat capacity of configurational subsystems	0.2822
Δc_1(J/(gK))	Coefficient of excess heat capacity of configurational subsystems	-0.0001112
a	Configurational contribution to the internal inelastic energy	0.5
$(\tau^g_{S_j}, \mu^{neq}_j)$	Discrete stress relaxation spectrum	Fig. 6(b)
$(\tau^g_{R_i}, \phi_i)$	Discrete structural relaxation spectrum	Fig. 7(b)
$(\tau^g_{N_j}, \mu^{back}_j)$	Discrete network relaxation spectrum	Fig. 10(a)
A(K)	Temperature coefficient	6154.3
V_S(cm^3/mol)	Activation volume for network relaxation	1474
m	Power of the orientation parameter	14.91
α_c	Cessation value of the orientation parameter for network relaxation	0.05
α_0	Initial value of the orientation parameter	0.616
λ_L	Limiting stretch	1.41

Table 3: Parameters of the constitutive model for polycarbonate.

Table. 3 lists the parameters, their physical significance and values determined for the polycarbonate material. We used the DMA, DSC, and specific aspects of the uniaxial compression stress-strain response at 37 °C and 95 °C to determine the model parameters as described below. The parameters were applied to predict the uniaxial compression response at 27 °C and 15 °C for model validation.

The nonequilibrium Young's modulus $E^{neq} = 1876.8$MPa was approximated by the maximum storage modulus of the master curve (Fig. 6a). The nonequilibrium shear modulus $\mu^{neq} = 695.1$ MPa and bulk modulus $\kappa = 2085.3$ MPa were calculated from E^{neq} assuming a glassy Poisson's ratio $\nu_g = 0.35$. The parameters of the discrete relaxation spectrum $\left(\tau^g_{S_j}, \mu^{neq}_j\right)$ at T_g (Fig. 6b), where $\tau^g_{S_j} = \nu^g_{S_j}/\mu^{neq}_j$, were fit to the master curve of the storage modulus (Fig. 6a) using the methods developed by Xiao and Nguyen [18] and Guo et al. [62] (Appendix B.1). The thermal activation parameters B and T_2 of the Adam-Gibbs model were determined by fitting to the temperature-dependence of the shift factor measured in the TTS test in the glass transition region (Fig. 6c) [19]. The DSC curve for the enthalpy change with temperature (Fig. 7a) was used to fit the discrete structural relaxation spectrum $(\tau_{R_i}, \mu^{neq}_i)$ at T_g (Fig. 7b) using the finite element model described in Sec. 2.2.5 and methods developed by Xiao and Nguyen [19] (Appendix B.2).

Figure 8 shows the experimentally measured uniaxial compression stress response plotted against the Gaussian hardening function $g(\lambda) = \left(1/\lambda - \lambda^2\right)$. The plots show the average and the variation of 3 tests at each strain rate and temperature. As expected, the stress response exhibits yielding, where the yield stress decreased with increasing temperature and decreasing strain rate, post-yield strain softening, followed by strain hardening. The strain hardening response was initially Gaussian, $\sigma = G_R g(\lambda)$, then became nonlinear. The Gaussian hardening region occurred earlier, at smaller strains, and extended over a larger strain range at 95 °C as illustrated in Figure 8.

The activation volume for local segmental relaxation V_Z was fit to the rate-dependence of the yield stress at 37 °C. The fraction parameter $0 < a < 1$, which controls the rate of strain-softening, was determined by fitting to the post-yield stress drop at 37°C for all the strain rates.

The activation volume for network relaxation $V_S = 860.63$ cm^3/mol and the parameters for the dependence of the network viscosities on the chain orientation α were determined from the rate-dependence of the backstress at 37°C. We approximated the backstress for the different strain rates at 4 true strains, 60 %, 70 %, 80 %, and 90 %, as the difference between the experimentally measured stress response and the model stress response without hardening. We further approximated the effective viscosity for network relaxation ν^N as the backstress divided by the applied true strain rate. From eq. (43), the relationship between ν^N, the effective back stress S^B, and chain orientation angle α for a given temperature can be expressed as, $\ln\left(1/\nu^N\right) = C(\alpha) - \ln\left(S^B\right) + \frac{V_S S^B}{RT}$, where $C(\alpha) = m\ln(\alpha) + \ln(\alpha - \alpha_c) + C_0$ and C_0 is a constant that depends on temperature and other model parameters. The activation volume V_S and $C(\alpha)$ for

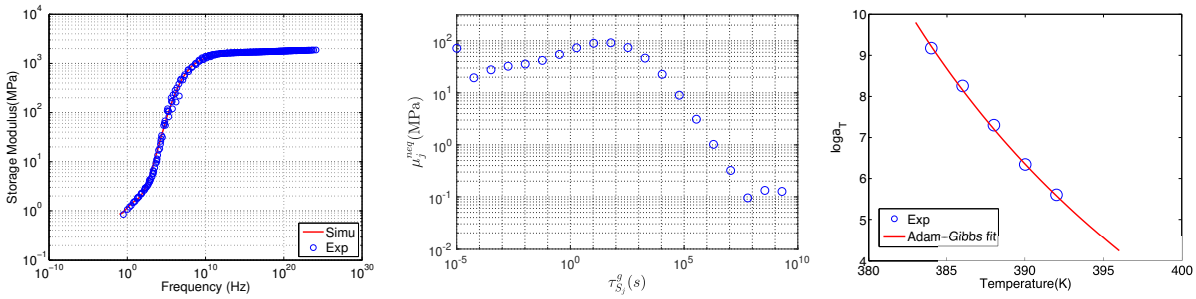

(b) (c)

Figure 6: (a) The master curve of the storage modulus obtained from time-temperature superposition for a reference temperature of $T_0 = 143°C$ was used to fit the (b) discrete stress relaxation spectrum $\left(\tau_{S_j}^g, \mu_j^{neq}\right)$ for $j = 1..20$ at T_g. (c) The temperature-dependent shift factor a_T was used to fit the parameters B and T_2 of the Adam-Gibbs model were fit to the temperature dependent shift factor a_T.

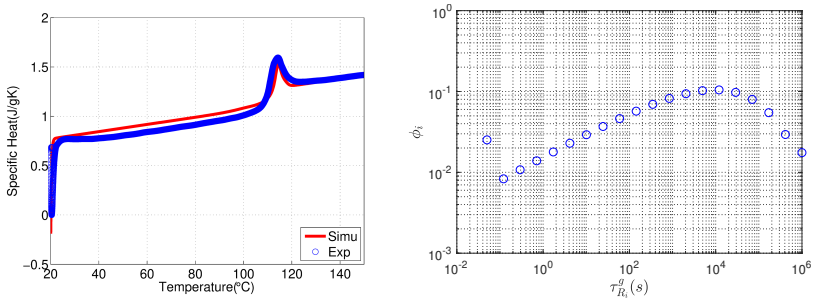

(b)

Figure 7: (a) The DSC curve was used to fit (b) the discrete structural relaxation spectrum $(\tau_{R_i}, \mu_i^{neq})$ for $i = 1..20$ at T_g.

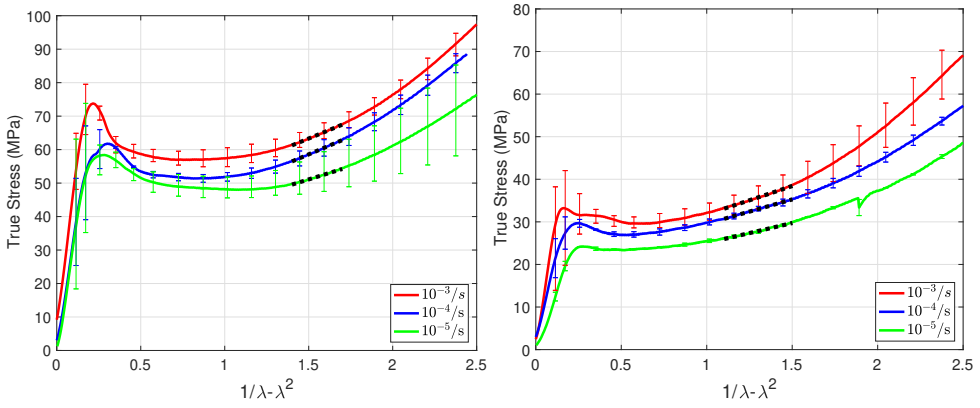

(a) (b)

Figure 8: The uniaxial compression stress response plotted against the Gaussian hardening function $g(\lambda) = \left(1/\lambda - \lambda^2\right)$ for polycarbonate specimens tested at (a)37°C and (b) 95°C and true strain rates 10^{-3}/s, 10^{-4}/s and 10^{-5}/s. The plots show the average of 3 tests for each strain rate and temperature with error bars showing the variations of 3 tests. The dashed black lines indicate the linear region of Gaussian hardening, $\sigma = G_R g(\lambda)$, used to determine the Gaussian hardening modulus G_R.

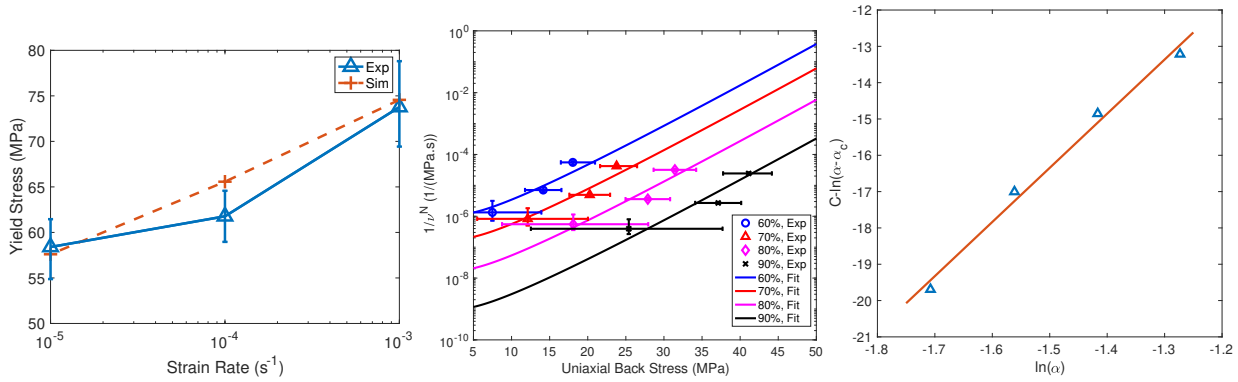

(a) (b) (c)

Figure 9: (a) The activation volume for segmental relaxation V_Z was fit to the rate-dependence of the yield stress at 37 °C. (b) The activation volume for network relaxation V_S and the factor C was fit to the network viscosity at 37 °C, 60 %, 70 %, 80 %, 90 % true strains, and $10^{-3}/s$, $10^{-4}/s$, $10^{-5}/s$ strain rates. (c) The power-law exponent for the dependence on the chain orientation was determined by fitting $C - \ln(\alpha - \alpha_c)$ at 60 %, 70 %, 80 %, 90 % true strains, 37 °C.

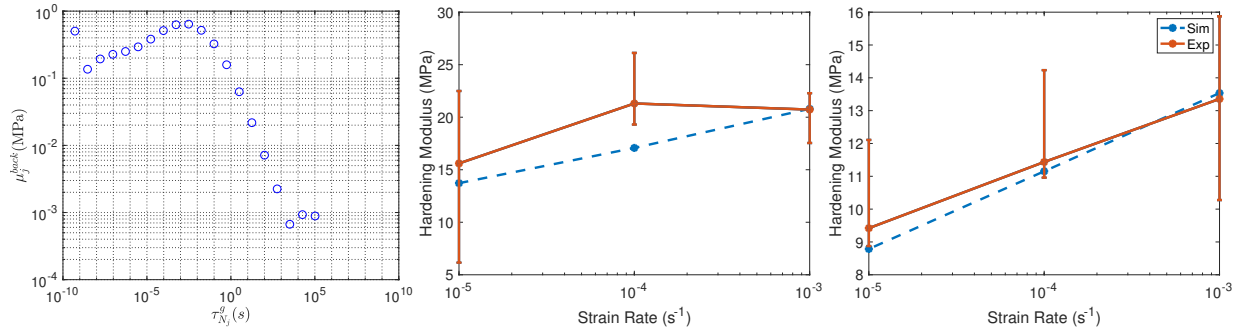

(a) (b) (c)

Figure 10: (a) The network relaxation spectrum $(\tau^g_{N_j}, \mu^{back}_j)$ for $j = 1..20$ at T_g was obtained by scaling the stress relaxation spectrum such that $\tau^g_{N_j} = d_1 \tau^g_{S_j}$ and $\mu^{back}_j = d_2 \mu^{neq}_j$. (b) The Gaussian hardening modulus G_R at 37°C for all strain rates was used to fit the scaling factors d_1 and d_2 of the network relaxation spectrum. (c) The G_R at 95°C and $10^{-3}/s$ was used to fit the thermal activation parameter A for network relaxation. The model was used to predict G_R at the lower strain rates $10^{-4}/s$ and $10^{-5}/s$ for model validation.

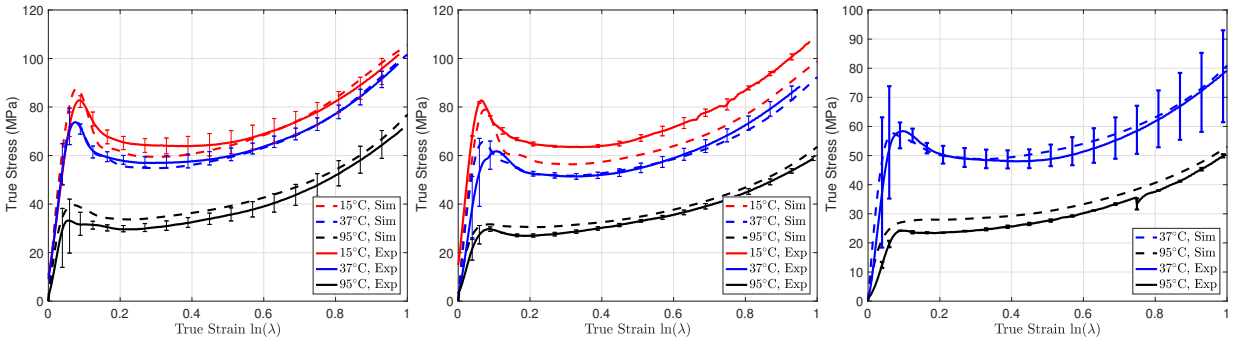

Figure 11: Uniaxial compression response of polycarbonate at 15 °C, 37 °C and 95 °C for different strain rates: (a)10^{-3}/s (b) 10^{-4}/s and (c) 10^{-5}/s. In general, the modeling resuls showed good agreement with experimental measurements of the uniaxial compression stress response for a wide range of temperatures and strain rates.

the 4 strains were fit to plots of $\ln\left(1/\nu^N\right)$ as a function of the backstress for the different strains and strain rates (Fig. 9c). The exponent m was determined from the slope of a line fit to a plot of $C(\alpha) - \ln(\alpha - \alpha_c)$ as a function of $\ln\alpha$. (Fig. 9d). The initial chain orientation angle $\alpha_0 = 0.616$ rad was calculated from the geometry of the 8-chain unit cube, and the critical chain orientation angle for the cessation of network relaxation was set to $\alpha_c = 0.05$ rad so that the corresponding 176.5 % critical strain was significantly greater than applied in the uniaxial compression test.

We assumed for simplicity that the network relaxation spectrum (Fig. 10a) can be approximated by scaling the stress relaxation spectrum, such that $\tau^g_{N_j} = d_1\tau^g_{S_j}$ and $\mu_j^{back} = d_2\mu_j^{neq}$. The scaling factors d_1 and d_2 were fit to the Gaussian hardening modulus G_R of the stress response at 37°C for the 3 strain rates (Fig. 10a). The G_R was determined as the slope of the stress plotted against the Gaussian hardening function $g(\lambda) = \left(1/\lambda - \lambda^2\right)$ in the linear range $g(\lambda) = 1.4$ to 1.7 (Fig. 8a). The activation energy $A = 6949.5$ K for the network viscosity was fit to G_R measured at 95 $^\circ C$ for the $10^{-3}/s$ strain rate (Fig. 10b). For 95 $^\circ C$, the Gaussian hardening region extended over the range $g(\lambda) = 1.1$ to 1.5 (Fig. 8b). Finally, the limiting stretch λ_L was determined from the strain at which the hardening stress responses transition from Gaussian hardening to a more nonlinear hardening.

4. Results

4.1. Uniaxial Compression

The uniaxial compression stress response at 15 °C, 37 °C and 95 °C are plotted in Fig. 11 for the different strain rates comparing the experimental data and modeling results. The stress response at 15 °C and for the lower strain rates $10^{-5}/s$ and $10^{-4}/s$ at 95 °C were not used to fit the model parameters. The model was able to capture the major features of the different regions of the average stress-strain response, including the rate-dependence and temperature-dependence of the yield peak, post-yield strain-softening and strain hardening. The model predictions for the Gaussian hardening modulus at 95 °C for the lower strain rates $10^{-5}/s$ and $10^{-4}/s$ were within 10 % of the experimental (Fig. 10c).

The model was applied to simulate the load-unload-reload uniaxial compression experiments at 27°C at 10^{-3}/s and 10^{-4}/s (Fig. 12) to further test the predictive capability of the model. A single sample was tested at each strain rate. As observed in experiments, the model exhibited strain recovery during unloading, which caused the reloading curve to be on the left of the unloading curve. The reloading stress response experienced yielding at the maximum stress before unloading, no post-yield stress drop because of mechanical rejuvenation, and a stiffer strain-hardening response that followed the hardening response of a specimen continuously loaded to the same total strain [42]. The model predicted a smaller strain recovery response during unloading, but otherwise showed good quantitative agreement with experiments for the 10^{-3}/s data. The stress response for the $10^{-4}/s$ strain rate experienced a sudden drop in the stress response before unloading, which led to large quantitative differences between the model and experimental results. However, the reloading stress response exhibited the same strain hardening modulus as the experiments.

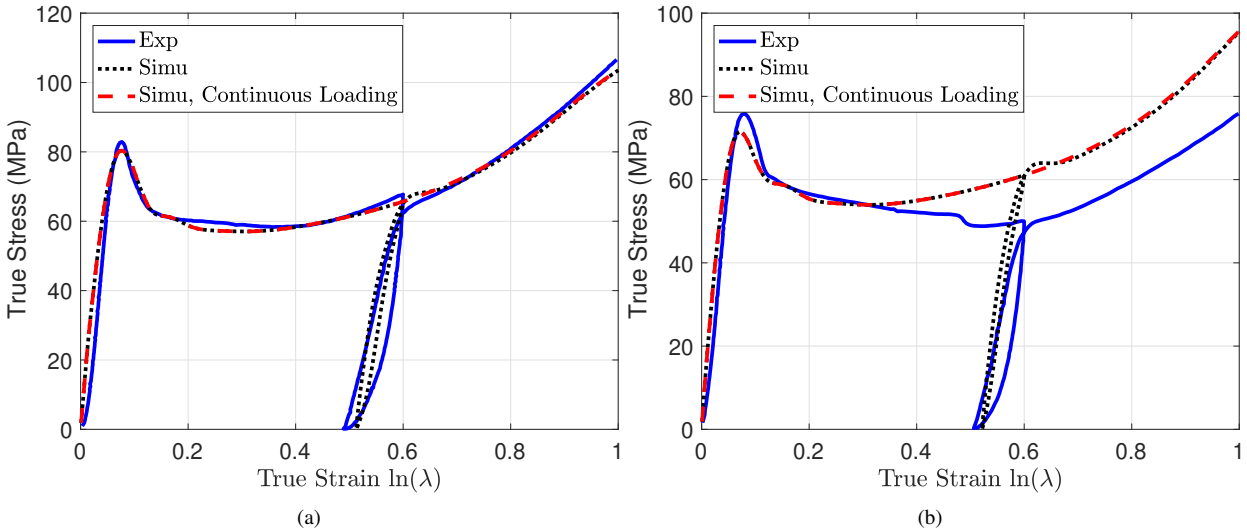

Figure 12: Loading-unloading-reloading response of polycarbonate specimens deformed at room temperature (27°C) and engineering strain rates of (a)10^{-3}/s and (b) 10^{-4}/s. The yield and post-yield stress response follows that of a specimen continuously deformed to the same total strain.

4.1.1. Parameter Study

We investigate the effects of the parameters of the network relaxation model in eq. (44) on the strain-hardening response. The activation temperature A controls the temperature dependence of strain hardening. To examine its effects, we compared the Gaussian hardening modulus for $A = 6154.3$K and $A = 10000$K (Fig. 13(a)). A larger value of A resulted in a larger hardening modulus and a stronger temperature dependence. We also compared the Gaussian hardening modulus for $V_S = 6651$ cm^3/mol and $V_S = 1474$ cm^3/mol for the same range of temperatures and strain rates (Fig. 13b). Decreasing the activation volume resulted in a larger hardening modulus and stronger strain rate dependence. The power-law exponent m describes the degree in which molecular orientation increases the resistance to network relaxation. A higher m produced a stiffer and more nonlinear hardening response (Fig. 13c). The parameter λ_L determines the nonlinear stiffening of the rate-independent backstress response at large strains. Decreasing λ_L decreased the transition strain between Gaussian and non-Gaussian hardening (Fig. 13d), which produced a stronger strain-stiffening effect after the transition strain but otherwise did not affect the strain-stiffening response in the Gaussian hardening region. The parameter d_1 describes the reference viscosity. Increasing d_1 increases the stress response slightly in both Gaussian hardening region and non-Gaussian hardening region.

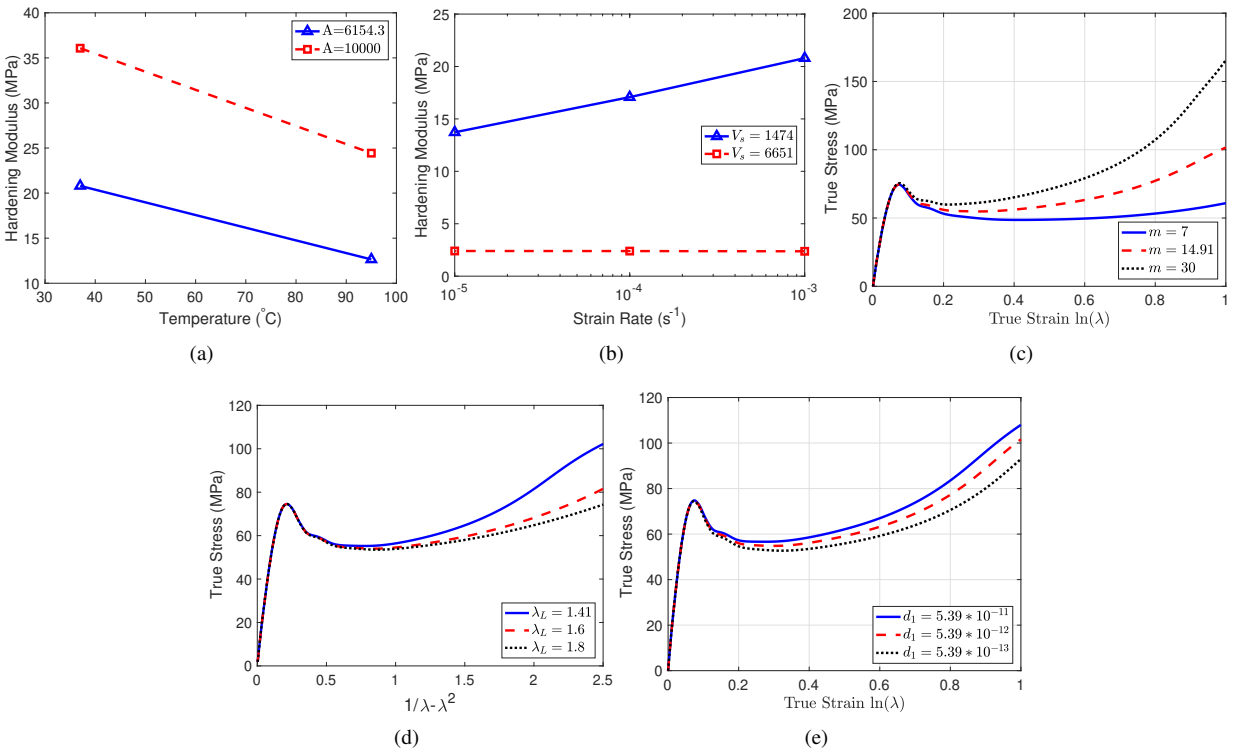

Figure 13: Effects of parameters that control the temperature, strain rate and strain state dependence of hardening (a) Hardening modulus at 37°C and 95°C with strain rate of 10^{-3}/s, for $A = 6949.5K$ and $A = 10000K$ respectively. (b) Hardening modulus at 10^{-3}/s, 10^{-4}/s and 10^{-5}/s with temperature of 37°C, for $V_S = 1474\text{cm}^3/\text{mol}$ and $V_S = 6651\text{cm}^3/\text{mol}$ respectively. (c) Stress response at 95°C and 10^{-3}/s, for $m = 7$, $m = 14.91$ and $m = 30$ respectively. (d). Stress response at 37 °C and 10^{-3}/s, for $\lambda_L = 1.41$, $\lambda_L = 1.6$, $\lambda_L = 1.8$ respectively. (e). Stress response at 37 °C and 10^{-3}/s, for d_1=5.39×10^{-11}, d_1=5.39×10^{-12}, d_1=5.39×10^{-13} respectively

4.2. Peel Simulation

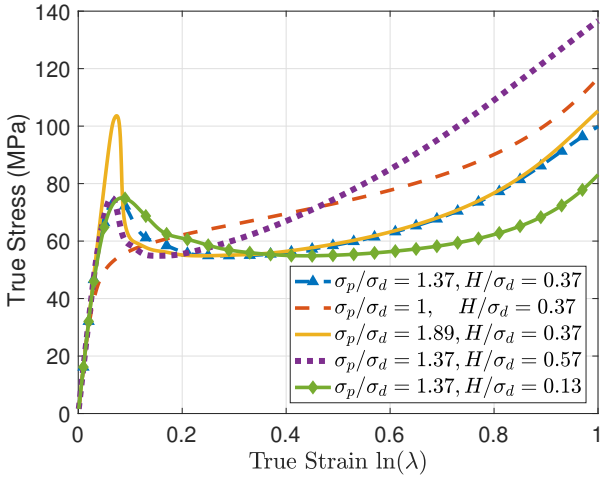

Figure 14: Uniaxial compression strain stress curves of material properties investigated in this section, 37°C 0.001/s true strain rate.

The effective temperature model and parameters determined for the polycarbonate material in Table 2 were applied to study for the effects of the post-yield stress drop and hardening modulus on 90° peeling of a single 3D-printed fiber from a rigid substrate. The uniaxial compression stress response corresponding to the different cases are shown in Fig. 14. The annealing time was varied in the simulation of the specimen before mechanical loading to vary the ratio of the peek stress to draw stress from 1 to 1.89. The post-yield stress drop for the highest ratio was 40 MPa larger than the lowest ratio. The parameters of the network relaxation were varied (Sec. 2.2.7) to produce a range of the hardening modulus normalized by the draw stress from 0.13 to 0.57.

The steady-state peel energy (Fig. 15(a)), intrinsic viscoplastic dissipation, viscoplastic dissipation from bending, and the rate of stored mechanical energy (Fig. 15(b)) decreased significantly with increasing ratio of the peak yield stress to the draw stress. Post-yield soften promotes localization of the plastic zone; thus a material with a greater post-yield stress drop exhibit a smaller plastic zone around the crack tip and at near the upper surface of the 90° bend (Fig. 17), which leads to a smaller intrinsic dissipation rate, bending dissipation rate, and stored mechanical energy release rate.

Increasing the ratio of the hardening modulus to the draw stress from 0.13 to 0.57 produced a small increase the tear energy from 1.49 Φ to 1.51 Φ, where Φ is the cohesive energy (Fig. 15(a)). For the parameters of the study, the maximum principle Euler-Almansi (true) strain in plastic zone was less than 15% for all cases (Fig. 16(c)), which corresponds to the post-yield stress drop in the viscoplastic stress response. Hardening develops at higher strains, near 30 % true strain. Thus, the mechanical behavior in front of the crack tip was dominated by post-yield softening response (Fig. 14) rather than strain hardening. This result was consistent with the findings of Tvergaard and coworkers [63] that the steady state mode 1 fracture toughness do not depend significantly on the hardening modulus when T_n^{max}/σ_d was not significantly larger than 1.

5. Discussion

We developed an effective temperature theory for the viscoplastic behavior of glassy polymers by incorporating the effects of kinematic hardening and relaxation of the hardening stress. The new theory inherits the ability of the original effective temperature theory of Xiao and Nguyen [19, 64] to accurately describe the rate-dependent and temperature-dependent yield and post-yield softening over a wide range of temperatures, including the glass transition region, the effects of physical aging and mechanical rejuvenation on the post-yield softening response, and the plastic heating deficit [21, 19]. The introduction of a viscoplatic backstress with a spectrum of relaxation processes allowed the new theory to capture the temperature-dependent and rate-dependent strain hardening behavior at larger strains.

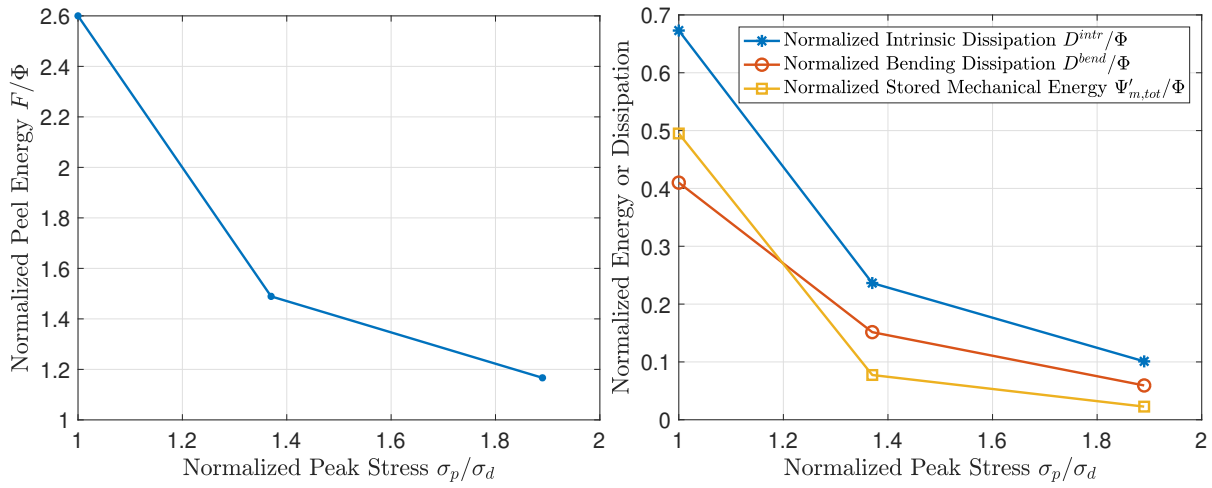

(a) (b)

Figure 15: The steady-state (a) peel energy F, (b) rate of intrinsic viscoplastic dissipation D^{intr}, rate of viscoplastic dissipation caused by bending D^{bend}, and rate of stored mechanical energy $\Psi_{,m,tot}$ normalized by the cohesive energy Φ for different ratios of peak stresses to draw stress. A larger ratio of the peak stress to draw stress produced a smaller normalized peel energy F/Φ, and smaller normalized intrinsic dissipation, bending dissipation and stored mechanical release rate.

The kinematic hardening formulation also allowed the model to accurately predict the viscoplastic behavior of a cold-worked (plastically pre-deformed) material, including the greater yield strength and hardening modulus. The model also captured the Bauschinger effect under a fully reversed strains and the development of an anisotropic yield stress and strain hardening response in a cold-worked material. The result is a predictive modeling tool for applications that involve large plastic deformation and a wide temperature range spanning the glass transition, such as traditional polymer processing, melt extrusion additive manufacturing, and fracture.

The network relaxation mechanism was introduced previously by Dupaix and Boyce [39] to capture the temperature-dependence, rate-dependence and strain-dependence of the post-yield hardening response. The network deformation and relaxation mechanism in the Dupaix and Boyce model acted in parallel with the mechanism for local segmental rearrangement that produced yielding and post-yield softening (Fig. 1c). We took an alternate approach and incorporated network deformation and relaxation as a viscoplastic backstress (Fig. 1d). This allows the model to capture the effects of the plastic pre-deformation history on the yield and post-yield hardening stress response. The same approach was used in the original elastic hardening model of Haward and Thackray [25] and Arruda and Boyce [41], and the viscoplastic hardening model of Hempel [40]. Compared to the model of Hempel [40], the present multi-process model incorporates the effect of the broad distribution of stress and structural relaxation times. More importantly, the effective temperature thermodynamic framework allows the model to describe the effects of plastic pre-deformation (mechanical rejuvenation) and aging on the yield stress and post-yield stress-drop.

The effective temperature viscoplastic model was applied to characterize the thermomechanical properties of a polycarbonate fiber used for FFF, a melt extrusion polymer additive manufacturing process, and to investigate the effects of the viscoplastic material behavior on peel tests of a single FFF printed fiber. The effect of viscoelasticity, plastic yield stress and hardening modulus have been examined widely in the literature for the cohesive failure of bulk materials and interfacial failure of thin films. In bulk materials, hardening prohibits plastic localization resulting in a more ductile failure process. In peel tests, plasticity increases the peel energy but the effect of hardening modulus is dependent on the cohesive energy and the cohesive strength relative to the yield strength of the bulk material [59, 60, 65]. We found that for the properties of the polycarbonate filament, the strain hardening response had a small effect on the peel energy, viscoplastic dissipation rate and rate of stored energy of viscoplastic work. Increasing the hardening modulus by a factor of 4.3 increased the peel energy by 1.3%. This was consistent with finite element analysis study of peeling of a power-law hardening material by Georgiou et. al. [65] that found a small effect of

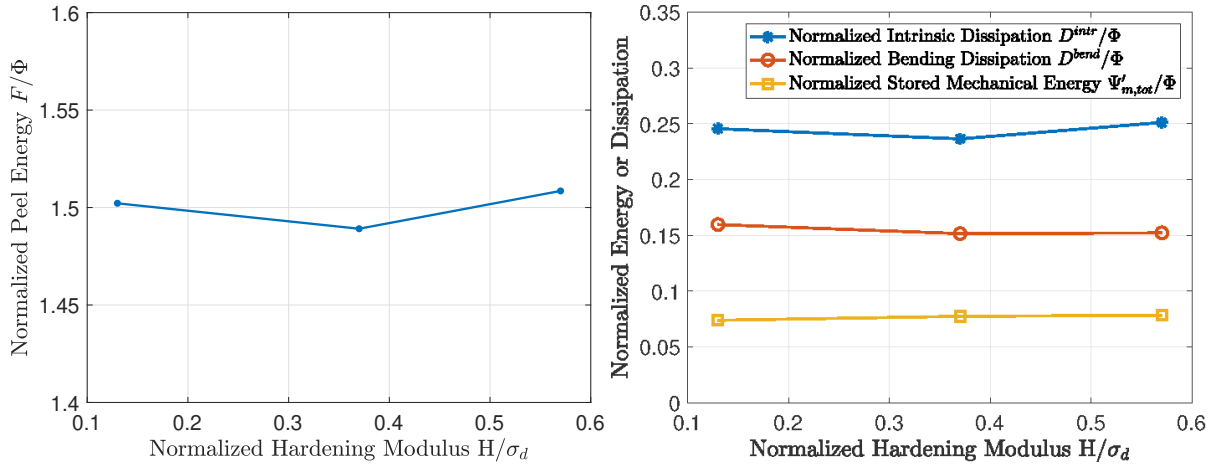

(a) (b)

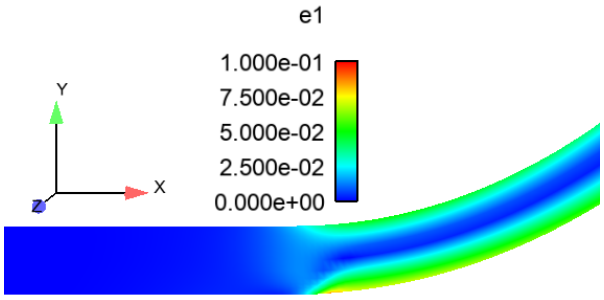

(c)

Figure 16: The steady-state (a) peel energy F, (b) rate of intrinsic viscoplastic dissipation D^{intr}, rate of viscoplastic dissipation caused by bending D^{bend}, and rate of stored mechanical energy $\Psi_{,m,tot}$ normalized by the cohesive energy Φ for different ratios of hardening modulus H to the draw stress. (c) Contour of maximum principle Green-Lagrange strain around crack tip, showing that the maximum strain did not exceed 15 %. Strain hardening is negligible at these strain levels, and the hardening modulus H does has a small effect on the peel energy, rate of viscoplastic dissipation and rate of mechanical stored energy.

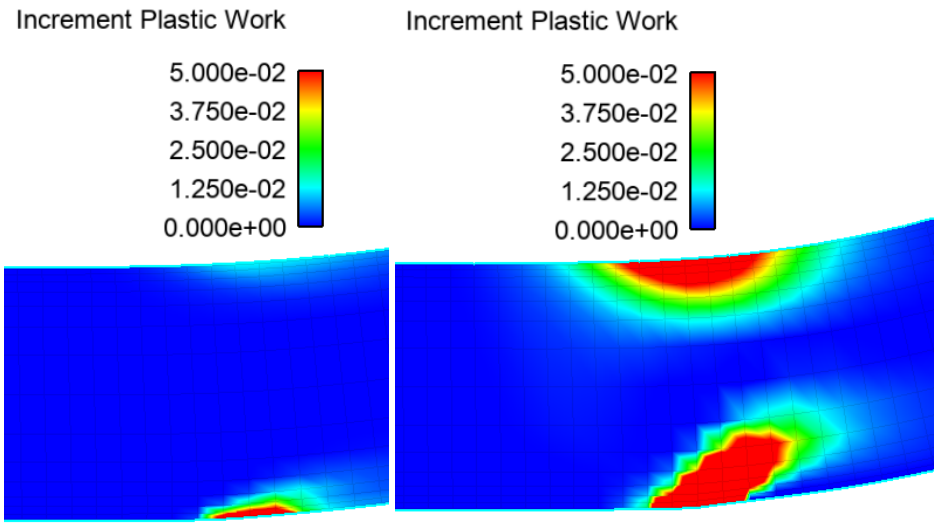

(a) (b)

Figure 17: The contour of the plastic dissipation $W^I + W^N$ (eqn. 50) at steady-state around crack tip for the case (a). $\sigma_p/\sigma_d = 1.89$, and the case (b). $\sigma_p/\sigma_d = 1$. The larger post-yield stress drop caused the plastic deformation to localize into a smaller zone ahead of the crack tip.

hardening. This trend might be sensitive to the magnitude of cohesive energy and maximum tractions in the cohesive zone model.

In contrast, the post-yield softening response had a significant effect on the peel energy and its contributions from viscoplastic dissipation and stored viscoplastic energy. The highest peel energy was obtained for a material behavior with no post-yield softening, and a smaller peel energy was obtained for a larger post-yield stress drop. Post-yield softening inhibited plastic dissipation and promoted increasingly localized plastic deformation. These results were consistent with the fact that physical aging embrittles glassy polymers [66, 67]. Moreover, polymers that exhibit a larger post-yield softening than hardening, such as polystyrene, exhibit brittle failure [68].

We are currently applying the findings of the peel simulation to design a peel test of a single FFF printed polycarbonate fiber to measure the effect of the printing history on the fiber-fiber welds. Among the main takeaways of the results is that the time in between printing and peel testing and the temperature variations during that storage time may be a significant source of variability in the measured peel force. In the future, we plan to fit the cohesive parameters from the experiment and provide a quantitative comparison on the effect of the printing conditions on the fracture energy of the printed welds.

The model presented here has a number of limitations. The model does not capture the effects of the hydrostatic pressure on the yield strength. It is well known that the yielding of glassy polymers is pressure dependent. For example, Spitzig and Richmond [69] showed that an applied confining pressure of 1104 MPa increases the yielding stress of polycarbonate from 64 MPa to 209 MPa. However, we don't expect such extreme hydrostatic pressures for the applications of filament deposition after melt extrusion. For uniaxial tension, the yield strength in compression is only 20% higher than in tension for polycarbonate [69]. Therefore, we did not include the effect of pressure in our model. However, this feature can be incorporated into the model by adding a pressure dependent term in V_Z, the activation volume for the viscous flow. The parameter can be fit to the asymmetry between the tension and compression stress-strain response.

We neglected the spatial conduction of the effective temperature for simulating the uniaxial compression tests and peel tests. We made the assumption because the configurational subsystems are slow to relax near T_g and are effectively frozen below the glass transition. Thus, the characteristic time for the disorder to diffuse becomes very long near T_g. However, this assumption preludes the model from capturing certain phenomena with a high gradient of plastic strain, such as the diffusive widening of shear bands [48]. For more discussion on the conduction of effective

temperature and its boundary conditions, the readers are referred to Manning et al. [70] and Bouchbinder and Langer [71].

For simplicity, we neglected the energy interactions between the configurational subsystems and assumed that the configurational properties, e,g. heat capacity, all had the same distribution over the Q configurational subsystems. The stress and structural relaxation processes were assumed to share the same dependence on the temperature and nonequilibrium structure. We have validated this assumption experimentally for a family of acrylate thermosets [19], but the assumptions need to be examined for a wider range of thermosets and thermoplastics.

In developing the model, we assumed that the internal elastic deformation gradients $\mathbf{F}^e$ and $\mathbf{F}^{ne}$ are coaxial, such that the nonequlibrium stress tensor τ^{NEQ} and the backstress tensor are coaxial. This simplified the numerical implementation of the model, but placed a severe restriction on the inelastic rotations, which may lead to unrealistic predictions for deformation states involving large rotations, such as simple shear. In future work, we plan to develop a more generalized model without these restrictions and associated numerical implementation that involves numerical integration of the full inelastic deformation tensor, see for example the work by Dettmer and Reese [72], and evaluate the errors introduced by this assumption.

We a applied a phenomenological model for the relaxation of the kinematic backstress, where the nonequilibrium configurational structure does not affect viscous resistance to kinematic hardening and kinematic hardening does not affect the evolution of the configurational structure (i.e., effective temperatures). Incorporating the dependence of the configuration structure in the viscous resistance to kinematic hardening produced a rate-dependence of strain hardening that was opposite to experimental observation. In the effective temperature theory, the evolution of the effective temperature approaches a stable nonequilibrium state after the post-yield stress drop, where the effect of mechanical rejuvenation from plastic work balances the structural relaxation process [64]. Without hardening, this would result in a stable draw stress. However, it is unclear if the molecular orientation achieved by the large plastic deformation process affects the configurational entropy and properties of the configurational subsystem. The large molecular orientation may also affect the viscous resistance to local segmental motion, which was not considered in the present work. The temperature dependence of the strain hardening response was achieved through the Arrhenius function and the activation energy A, which does not have a clear physical significance. Finally, we assumed that the relaxation spectrum for the hardening stress can be obtained through vertical and horizontal scaling of the stress relaxation spectrum. This assumption greatly simplified the parameter determination process and it seems to be appropriate based on the model's performance in describing the uniaxial compression stress response of polycarbonate. However, a more accurate method is needed to the characterize the network relaxation mechanism.

6. Conclusions

In conclusion, we developed an effective temperature theory model for the viscoplastic behavior of glassy polymers with strain hardening that incorporates a broad spectrum of structural relaxation, stress relaxation, and relaxation of the backstress. The model can capture a wide range of nonequilibrium behaviors including the rate-dependent yield, post-yield softening, and strain harding response over a wide range of temperatures; the effects of physical aging and mechanical rejuvenation on the post-yield softening response and the stress response upon reloading. The model was calibrated for a polycarbonate material for FFF additive manufacturing and applied to investigate the effects of the post-yield stress drop and hardening modulus on the peel energy and associated viscoplastic dissipation. The simulations showed that a larger post-yield stress drop inhibits plastic deformation and decreased the peel energy while the hardening modulus had little effect on plastic dissipation and the peel energy.

Appendix A. Kinetic vs. configurational contributions of the network resistance

This section examines the effects of replacing the Arrhenius model for the temperature-dependence of the network viscosities in eq. (44) with the Adam-Gibbs model for the temperature-dependence and structure-dependence:

$$\nu_j^N = \nu_j^{N,ref} \exp\left(\frac{B^N}{T\sum_i^Q \eta_i^c}\right)\left(\frac{\alpha_0-\alpha_c}{\alpha-\alpha_c}\right)\alpha^{-m}\frac{V_S S_{back}}{RT}\left[\sinh\left(\frac{V_S S_{back}}{RT}\right)\right]^{-1}, \tag{A.1}$$

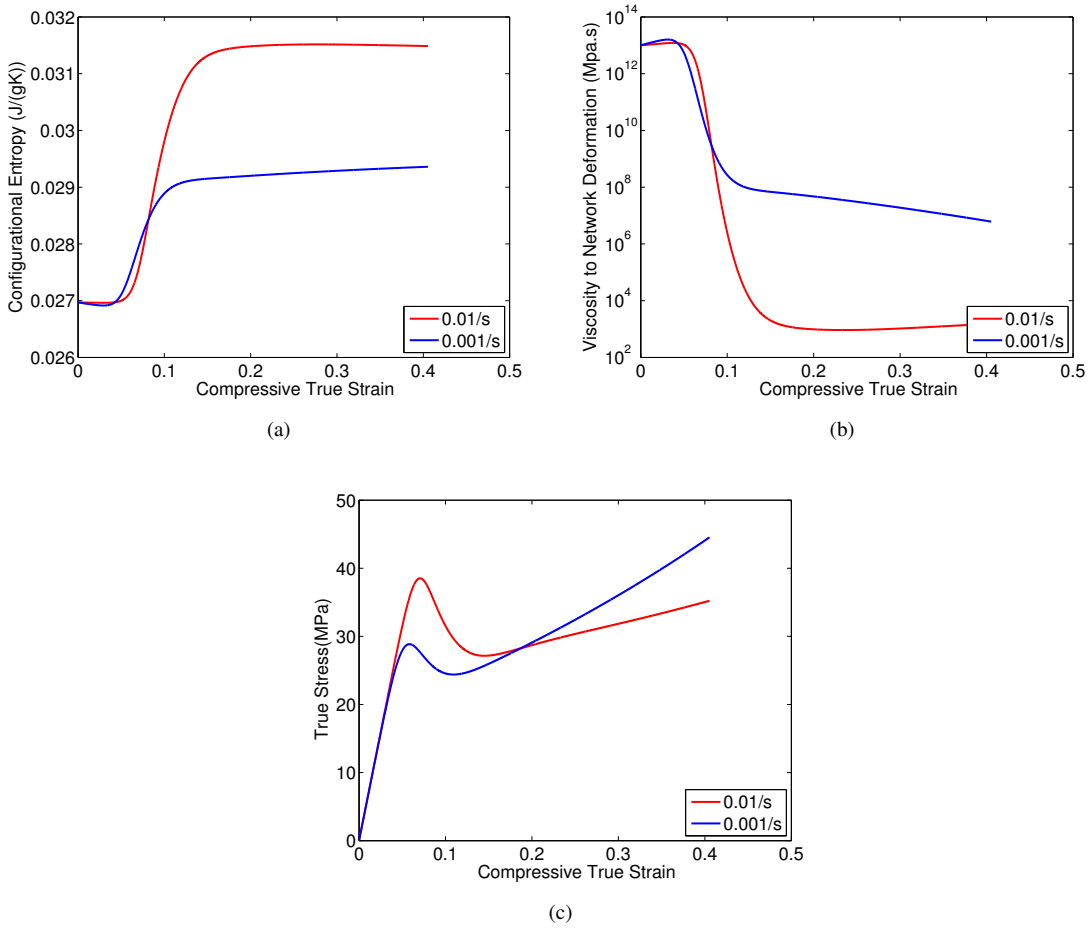

Figure A.18: Incorporating the Adam-Gibbs model for the temperature-dependence and structure-dependence of the viscous resistance to network deformation and simulating the uniaxial compression response at 95 °C, comparing the (a) evolution of configurational entropy, (b) evolution of viscous resistance to network deformation and (c) stress-strain curves for two strain rates, 10^{-2}/s and 10^{-3}/s. Incorporating the configurational structure led to a smaller hardening at the higher strain rate, which is opposite from experiments.

where B^N is the activation energy analogous to B in eq. (43). The model was applied to simulate uniaxial compression at 95 °C and two strain rates, 0.01/s and 0.001/s, to determine effects of the structural dependence on the rate-dependence of the hardening modulus. Upon yielding, mechanical rejuvenation from the disordering effects of the viscoplastic dissipation caused the configurational entropy to increase to a steady-state value. The larger strain rate imparted a greater disordering effect and higher steady-state configurational entropy (Fig. A.18a), which led to a more mobile chains and lower network viscosity (Fig. A.18b). This caused the hardening modulus to be smaller at the higher strain rate, which was the opposite observed in experiments.

As a results, we decided to omit the dependence of the v_j^N on the configurational structure, which made the network relaxation mechanism and the backstress independent of the effective temperatures. Configurational contributions of the network resistance can affect the evolution of the effective temperatures, but have little effects on the hardening stress response. This is demonstrated in Fig. A.19, where we simulated the uniaxial compression response at 95°C and engineering strain rate of 3×10^{-4}/s. The contributions of network resistance were either all assigned in the kinetic subsystem, which gives eq. (37) for $\dot{T}$ in the present model, or all assigned in the configurational subsystems, which would add to eq. (38) for $\dot{T}_i^e$. The stress response for both cases were nearly identical (Fig. A.19), we assumed pure kinematic contributions.

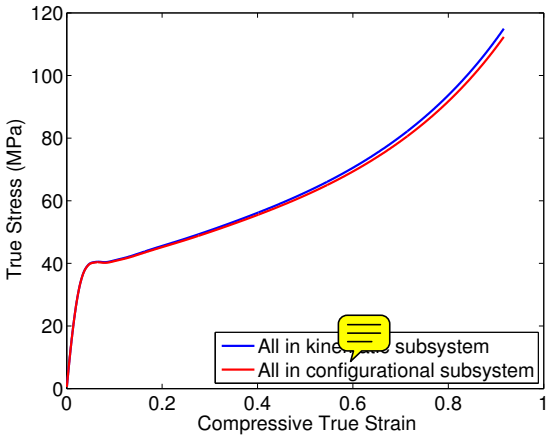

Figure A.19: Comparison of the stress response between pure kinematic and pure configurational contributions of network resistance.

Appendix B. Parameter Determination

Appendix B.1. Determining the stress relaxation spectrum

We applied the method developed by Xiao and Nguyen [18] to determine relaxation spectrum $\left(\tau_{S_j}^g, \mu_j^{neq}\right)$ of the undeformed material $\mathbf{F}=\mathbf{I}$ in equilibrium at $T=T_{e_i}=T_g$. From eq. (43), we can express the stress relaxation times at any temperature T in terms of $\tau_{S_j}^g$,

$$\tau_{S_j} = {\tau_{S_j}}^g \exp\left(\frac{B}{T\eta^c(T_{e_i},\mathbf{C})} - \frac{B}{T_g\eta^c(T_g,\mathbf{I})}\right)\frac{V_S^I S}{RT}\left[\sinh\left(\frac{V_S^I S}{RT}\right)\right]^{-1}. \tag{B.1}$$

Here η^c can be evaluated from eq. (15) as,

$$\begin{aligned}\eta^c(T_{e_i},\mathbf{C}) &= \sum_i^Q \eta_i^c \\ &= \sum_i^Q \left(\Delta c_0 \phi_i \log\frac{T_{e_i}}{T_2} + \Delta c_1 \phi_i (T_{e_i}-T_2) - \frac{\phi_i}{T_0}\frac{\mu^{eq}}{2}(\mathrm{tr}(\overline{\mathbf{C}})-3)\right).\end{aligned} \tag{B.2}$$

The ${\tau_{S_j}}^g$ and μ_j^{neq} were determined from the master curve of storage modulus. The storage modulus measured at different temperatures was plotted on a log-log scale in Fig. 6a and shifted horizontally to a reference temperature $T_0 = 143^\circ$C to form the master curve for the frequency-dependence of the storage modulus as shown in Fig. 6b. We determined the temperature range of the glass transition region by finding the range of the shift factor $a_T(T)$ that can be fitted to the WLF function (Fig. B.20). This gave $T_g = 110^\circ$C for the onset temperature and $C_1^0 = 9.7136$ and $C_2^0 = 65.572$K at reference temperature.

We developed a second-order approximation method based on Schwarzl and Staverman [73] to determine the discrete relaxation spectrum [62]. We first used a polynomial function denoted as $\log G' = f_0(\log\omega)$ to fit the master curve in Fig. 6b, where G' is the storage modulus and ω represents the angular frequency. The relation between relaxation modulus and a continuous relaxation spectrum was defined as [47],

$$G(t) = \mu^{eq} + \int_0^\infty h(\nu)e^{-\nu t}d\nu, \tag{B.3}$$

where $h(\nu)$ is the continuous relaxation spectrum. The cumulative relaxation spectrum is defined from $h(\nu)$ as,

$$H(\nu) = \int_0^\nu h(z)dz. \tag{B.4}$$

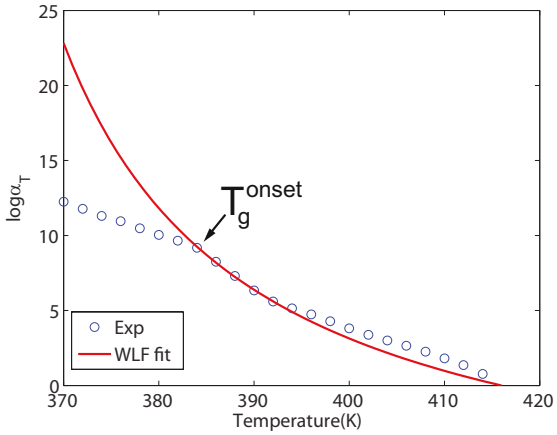

Figure B.20: The WLF function was fit to the temperature-dependent shift factor $a_T(T)$. The onset $T_g = 110$ °C was determined from the lowest temperature for which WLF can be fitted to a_T.

Evaluating $h(\nu)$ requires inverting the integral equation (B.3) which can be challenging. A number of approximations have been developed. In particular, we used a second-order accurate approximation developed by Schwarzl and Staverman [73],

$$\begin{aligned} h(\nu) = \tfrac{\sqrt{2}}{\omega} G'(\omega)[d\log G'/d\log\omega - \tfrac{1}{2}(d\log G'/d\log\omega)^2 \\ -\tfrac{1}{4.606} d^2\log G'/d(\log\omega)^2]|_{\omega=\sqrt{2}\nu}. \end{aligned} \quad . \tag{B.5}$$

Applying the polynomial fit to eqs. (B.5) and (B.4), we can calculate the continuous relaxation spectrum and cumulative distribution from polynomial function f_0 as,

$$h(\nu) = 10^{f_0(x)-x}\sqrt{2}(f_0{}'(x) - \frac{1}{2}(f_0{}'(x))^2 - \frac{1}{4.606} f_0{}''(x))|_{x=\log\sqrt{2}\nu}, \tag{B.6}$$

$$H(\nu) = 10^{f_0(x)}(1 - \frac{1}{2} f_0{}'(x))|_{x=\log\sqrt{2}\nu}. \tag{B.7}$$

The relaxation modulus of the discrete model can be written as,

$$G_{disc}(t) = \mu^{eq} + \sum_j^P \mu_j^{neq} \exp(-t\nu_j). \tag{B.8}$$

The discrete cumulative spectrum can be evaluated by combining eqs. (B.3), (B.4) and (B.8) as,

$$H_{disc}(\nu) = \sum_j^P \mu_j^{neq} \langle \nu - \nu_j \rangle^1 - \mu^{eq}, \tag{B.9}$$

where $\langle\rangle^1$ denotes a step function. We then assume a power law distribution for the relaxation frequencies,

$$\nu_j^0 = \nu_{\min}^0 \left(\frac{\nu_{\max}^0}{\nu_{\min}^0} \right)^{(j-1)/(P-1)}, \tag{B.10}$$

where $\nu_{\max}^0$ and $\nu_{\min}^0$ are the maximum and minimum of relaxation frequencies and are selected based on the frequency range of the master curve. Finally, the nonequilibrium moduli μ_j^{neq} corresponding to the relaxation frequencies ν_j^0 were determined from the continuous cumulative distribution as follows [74, 46],

$$\begin{aligned} \mu_1^{neq} &= \tfrac{1}{2}(H(\nu_1^0) + H(\nu_2^0)), \\ \mu_j^{neq} &= \tfrac{1}{2}(H(\nu_{j+1}^0) - H(\nu_{j-1}^0)), 1 < j < P-1, \\ \mu_P^{neq} &= \mu^{neq} - \sum_j^{P-1} \mu_j^{neq}. \end{aligned} \tag{B.11}$$

The stress relaxation time ${\tau^g}_{S_j}$ can be evaluated from ν_j^0,

$$ {\tau^g}_{S_j} = \frac{1}{\nu_j^0} \exp\left(\frac{B}{T_g \eta^c(T_g, \mathbf{I})} - \frac{B}{T_0 \eta^c(T_0, \mathbf{I})} \right). \tag{B.12} $$

Fig. 7a plots the stress relaxation spectrum $(\tau_{S_j}^g, \mu_j^{neq})$ with $P = 20$ processes determined as described above. The spectrum was applied to evaluate the storage modulus of the discrete model,

$$ E'(\omega) = E^{eq} + \sum_j^P \frac{E_j^{neq} \omega^2 / (\nu_j^0)^2}{1 + \omega^2 / (\nu_j^0)^2}. \tag{B.13} $$

The results shown in Fig. B.21 show excellent agreement with the measured master curve.

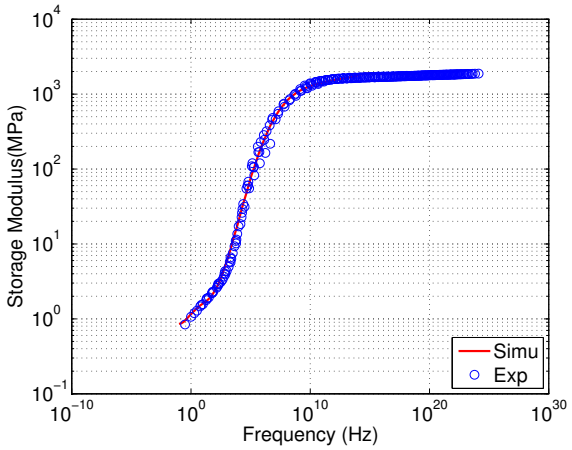

Figure B.21: Comparison of the experimentally measured master curves and the fit of the discrete model.

Appendix B.2. Determining the structural relaxation spectrum and heat capacities

Similar to Sec. Appendix B.1, we aimed to determine $\tau_{R_i}^g$, which is the structural relaxation time at glass transition temperature and no deformation, in this subsection. And from eq.(45), the structural relaxation time in the general case can be expressed as,

$$ \tau_{R_i} = {\tau_{R_i}}^g \exp\left(\frac{B}{T \eta^c(T_{e_i}, \mathbf{C})} - \frac{B}{T_g \eta^c(T_g, \mathbf{I})}\right). \tag{B.14} $$

To determine the structural $\tau_{R_i}^g$ and ϕ_i, we first assumed that the structural relaxation spectrum can be described by the Kohlrausch-Williams-Watts (KWW) model [18, 19] and then discretize this continuous spectrum to get $\tau_{R_i}^g$ and ϕ_i. The KWW model can be expressed as infinite series [75],

$$ h_{KWW}(\tau) = -\frac{\chi}{\pi \tau^2} \sum_{k=0}^{\infty} \frac{(-1)^k}{k!} \sin(\pi \beta k) \Gamma(\beta k + 1) \left(\frac{\tau}{\chi}\right)^{\beta k + 1}, \tag{B.15} $$

where χ is the characteristic structural relaxation time, $0 \leq \beta \leq 1$ represents the breadth of the structural relaxation spectrum and $\Gamma()$ is the gamma function. We also assumed a power law distribution for discrete structural relaxation times,

$$ \tau_{R_i}^g = \tau_{\min} \left(\frac{\tau_{\max}}{\tau_{\min}}\right)^{(i-1)/(Q-1)}. \tag{B.16} $$

The discrete structural relaxation spectrum were determined by a stepwise approximation of the cumulative relaxation spectrum $H_{KWW}(\tau) = \int_0^\tau h_{KWW}(t)dt$ as,

$$\begin{aligned}
&\phi_1 = \tfrac{1}{2}(H_{KWW}(\tau^g{}_{R_1}) + H_{KWW}(\tau^g{}_{R_2})),\\
&\phi_i = \tfrac{1}{2}(H_{KWW}(\tau^g{}_{R_{i+1}}) - H_{KWW}(\tau^g{}_{R_{i-1}})), 1 < i < Q-1,\\
&\phi_Q = 1 - \sum_i^{Q-1} \phi_i.
\end{aligned} \tag{B.17}$$

We simulated the DSC experiments using the method in 2.2.5 and tuned the characteristic time $\chi = 5000$s and breadth $\beta = 0.30$ to fit the position, width and height of the DSC endothermic overshoot (Fig. B.22)).

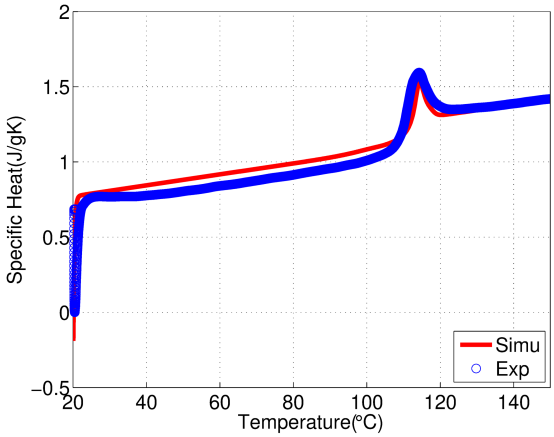

Figure B.22: Comparison between the measured and model predicted DSC response.

The coefficients for heat capacities can be obtained through linear fits of the DSC curve in different temperature ranges. Specifically, the kinetic components c_{g0} and c_{g1} were determined from a linear fit of the DSC curve from 40°C to 60°C, while the heat capacity for the whole system was determined from a linear fit of the DSC curve from 130°C to 150°C. Subtracting the kinetic components from the heat capacity of the whole system gives the configurational components of heat capacity Δc_0 and Δc_1.

References

[1] M. Boyce, R. Haward, The post-yield deformation of glassy polymers, in: The physics of glassy polymers, Springer, 1997, pp. 213–293.

[2] E. M. Arruda, Characterization of the strain hardening response of amorphous polymers, Ph.D. thesis, Massachusetts Institute of Technology (1992).

[3] T. A. Tervoort, Constitutive modelling of polymer glasses: finite, nonlinear viscoelastic behaviour of polycarbonate, Eindhoven University of Technology Eindhoven, 1996.

[4] H. Van Melick, L. Govaert, H. Meijer, On the origin of strain hardening in glassy polymers, Polymer 44 (8) (2003) 2493–2502.

[5] R. S. Hoy, M. O. Robbins, Strain hardening of polymer glasses: effect of entanglement density, temperature, and rate, Journal of Polymer Science Part B: Polymer Physics 44 (24) (2006) 3487–3500.

[6] E. M. Arruda, M. C. Boyce, R. Jayachandran, Effects of strain rate, temperature and thermomechanical coupling on the finite strain deformation of glassy polymers, Mechanics of Materials 19 (2-3) (1995) 193–212.

[7] L. Govaert, T. Tervoort, Strain hardening of polycarbonate in the glassy state: influence of temperature and molecular weight, Journal of Polymer Science Part B: Polymer Physics 42 (11) (2004) 2041–2049.

[8] H. Eyring, Viscosity, plasticity, and diffusion as examples of absolute reaction rates, The Journal of chemical physics 4 (4) (1936) 283–291.

[9] T. Ree, H. Eyring, Theory of non-newtonian flow. i. solid plastic system, Journal of Applied Physics 26 (7) (1955) 793–800. arXiv:https://doi.org/10.1063/1.1722098, doi:10.1063/1.1722098.
URL https://doi.org/10.1063/1.1722098

[10] A. S. Argon, A theory for the low-temperature plastic deformation of glassy polymers, The Philosophical Magazine: A Journal of Theoretical Experimental and Applied Physics 28 (4) (1973) 839–865. arXiv:https://doi.org/10.1080/14786437308220987, doi:10.1080/14786437308220987.
URL https://doi.org/10.1080/14786437308220987

[11] O. Hasan, M. Boyce, A constitutive model for the nonlinear viscoelastic viscoplastic behavior of glassy polymers, Polymer Engineering & Science 35 (4) (1995) 331–344.

[12] E. Klompen, T. Engels, L. Govaert, H. Meijer, Modeling of the postyield response of glassy polymers: influence of thermomechanical history, Macromolecules 38 (16) (2005) 6997–7008.

[13] H. E. Meijer, L. E. Govaert, Mechanical performance of polymer systems: The relation between structure and properties, Progress in polymer science 30 (8-9) (2005) 915–938.

[14] R. Xiao, T. D. Nguyen, A thermodynamic modeling approach for dynamic softening in glassy amorphous polymers, Extreme Mechanics Letters 8 (2016) 70 – 77, nanomechanics: Bridging Spatial and Temporal Scales. doi:https://doi.org/10.1016/j.eml.2016.03.005.
URL http://www.sciencedirect.com/science/article/pii/S2352431615300493

[15] C. Buckley, P. Dooling, J. Harding, C. Ruiz, Deformation of thermosetting resins at impact rates of strain. part 2: constitutive model with rejuvenation, Journal of the Mechanics and Physics of Solids 52 (10) (2004) 2355 – 2377. doi:https://doi.org/10.1016/j.jmps.2004.04.001.
URL http://www.sciencedirect.com/science/article/pii/S0022509604000742

[16] H. Li, C. Buckley, Necking in glassy polymers: effects of intrinsic anisotropy and structural evolution kinetics in their viscoplastic flow, International Journal of Plasticity 26 (12) (2010) 1726–1745.

[17] J. Choi, A. M. Ortega, R. Xiao, C. M. Yakacki, T. D. Nguyen, Effect of physical aging on the shape-memory behavior of amorphous networks, Polymer (Guildf). 53 (12) (2012) 2453–2464. doi:10.1016/j.polymer.2012.03.066.
URL http://linkinghub.elsevier.com/retrieve/pii/S0032386112003035

[18] R. Xiao, J. Choi, N. Lakhera, C. M. Yakacki, C. P. Frick, T. D. Nguyen, Modeling the glass transition of amorphous networks for shape-memory behavior, Journal of the Mechanics and Physics of Solids 61 (7) (2013) 1612–1635.

[19] R. Xiao, T. D. Nguyen, An effective temperature theory for the nonequilibrium behavior of amorphous polymers, Journal of the Mechanics and Physics of Solids 82 (2015) 62–81.

[20] R. Xiao, C. Tian, A constitutive model for strain hardening behavior of predeformed amorphous polymers: Incorporating dissipative dynamics of molecular orientation, Journal of the Mechanics and Physics of Solids 125 (2019) 472 – 487. doi:https://doi.org/10.1016/j.jmps.2019.01.008.
URL http://www.sciencedirect.com/science/article/pii/S0022509618309517

[21] R. Xiao, G. Ghazaryan, T. A. Tervoort, T. D. Nguyen, Modeling energy storage and structural evolution during finite viscoplastic deformation of glassy polymers, Physical Review E 95 (6) (2017) 063001.

[22] G. Adam, J. H. Gibbs, On the temperature dependence of cooperative relaxation properties in glass-forming liquids, The journal of chemical physics 43 (1) (1965) 139–146.

[23] G. W. Scherer, Use of the adam-gibbs equation in the analysis of structural relaxation, Journal of the American Ceramic Society 67 (7) (1984) 504–511.

[24] R. Xiao, T. D. Nguyen, A thermodynamic modeling approach for dynamic softening in glassy amorphous polymers, Extreme Mechanics Letters 8 (2016) 70 – 77, nanomechanics: Bridging Spatial and Temporal Scales. doi:https://doi.org/10.1016/j.eml.2016.03.005.
URL http://www.sciencedirect.com/science/article/pii/S2352431615300493

[25] R. Haward, G. . Thackray, The use of a mathematical model to describe isothermal stress-strain curves in glassy thermoplastics, Proc. R. Soc. Lond. A 302 (1471) (1968) 453–472.

[26] T. Tervoort, L. Govaert, Strain-hardening behavior of polycarbonate in the glassy state, Journal of Rheology 44 (6) (2000) 1263–1277.

[27] M. C. Wang, E. Guth, Statistical theory of networks of non-gaussian flexible chains, The Journal of Chemical Physics 20 (7) (1952) 1144–1157.

[28] E. M. Arruda, M. C. Boyce, A three-dimensional constitutive model for the large stretch behavior of rubber elastic materials, Journal of the Mechanics and Physics of Solids 41 (2) (1993) 389–412.

[29] H. M. James, E. Guth, Theory of the elastic properties of rubber, The Journal of Chemical Physics 11 (10) (1943) 455–481.

[30] M. C. Boyce, D. M. Parks, A. S. Argon, Large inelastic deformation of glassy polymers. part i: rate dependent constitutive model, Mechanics of Materials 7 (1) (1988) 15–33.

[31] M. Boyce, E. Arruda, An experimental and anaiytical investigation of the large strain compressive and tensile response of glassy polymers, Polymer Engineering & Science 30 (20) (1990) 1288–1298.

[32] D. Lee, P. C. Luken, Material modeling and solid phase forming of polycarbonate sheet, Polymer Engineering & Science 26 (9) (1986) 612–619. arXiv:https://onlinelibrary.wiley.com/doi/pdf/10.1002/pen.760260906, doi:10.1002/pen.760260906.
URL https://onlinelibrary.wiley.com/doi/abs/10.1002/pen.760260906

[33] M. Mooney, A theory of large elastic deformation, Journal of Applied Physics 11 (9) (1940) 582–592. arXiv:https://doi.org/10.1063/1.1712836, doi:10.1063/1.1712836.
URL https://doi.org/10.1063/1.1712836

[34] R. S. Rivlin, E. K. Rideal, Large elastic deformations of isotropic materials iv. further developments of the general theory, Philosophical Transactions of the Royal Society of London. Series A, Mathematical and Physical Sciences 241 (835) (1948) 379–397. arXiv:https://royalsocietypublishing.org/doi/pdf/10.1098/rsta.1948.0024, doi:10.1098/rsta.1948.0024.
URL https://royalsocietypublishing.org/doi/abs/10.1098/rsta.1948.0024

[35] P. Wu, E. Van Der Giessen, On improved network models for rubber elasticity and their applications to orientation hardening in glassy polymers, Journal of the Mechanics and Physics of Solids 41 (3) (1993) 427–456.

[36] J. Bergström, M. Boyce, Constitutive modeling of the large strain time-dependent behavior of elastomers, Journal of the Mechanics and Physics of Solids 46 (5) (1998) 931–954.

[37] L. E. Govaert, P. H. M. Timmermans, W. A. M. Brekelmans, The influence of intrinsic strain softening on strain localization in polycarbonate: Modeling and experimental validation, Journal of Engineering Materials and Technology 122 (2) (1999) 177–185.
URL http://dx.doi.org/10.1115/1.482784

[38] C. Buckley, D. Jones, Glass-rubber constitutive model for amorphous polymers near the glass transition, Polymer 36 (17) (1995) 3301 – 3312. doi:https://doi.org/10.1016/0032-3861(95)99429-X.
URL http://www.sciencedirect.com/science/article/pii/003238619599429X

[39] R. B. Dupaix, M. C. Boyce, Constitutive modeling of the finite strain behavior of amorphous polymers in and above the glass transition, Mechanics of Materials 39 (1) (2007) 39–52.

[40] P. Hempel, Constitutive modeling of amorphous thermoplastic polymers with special emphasis on manufacturing processes, Vol. 2, KIT Scientific Publishing, 2016.

[41] E. M. Arruda, M. C. Boyce, Evolution of plastic anisotropy in amorphous polymers during finite straining, International Journal of Plasticity 9 (6) (1993) 697 – 720. doi:https://doi.org/10.1016/0749-6419(93)90034-N.
URL http://www.sciencedirect.com/science/article/pii/074964199390034N

[42] D. Senden, J. Van Dommelen, L. Govaert, Strain hardening and its relation to bauschinger effects in oriented polymers, Journal of Polymer Science Part B: Polymer Physics 48 (13) (2010) 1483–1494.

[43] S. Raha, P. Bowden, Birefringence of plastically deformed poly(methyl methacrylate), Polymer 13 (4) (1972) 174 – 183. doi:https://doi.org/10.1016/0032-3861(72)90042-0.
URL http://www.sciencedirect.com/science/article/pii/0032386172900420

[44] M. Boyce, S. Socrate, P. Llana, Constitutive model for the finite deformation stress–strain behavior of poly(ethylene terephthalate) above the glass transition, Polymer 41 (6) (2000) 2183 – 2201. doi:https://doi.org/10.1016/S0032-3861(99)00406-1.
URL http://www.sciencedirect.com/science/article/pii/S0032386199004061

[45] P. Dooling, C. Buckley, S. Rostami, N. Zahlan, Hot-drawing of poly (methyl methacrylate) and simulation using a glass–rubber constitutive model, Polymer 43 (8) (2002) 2451–2465.

[46] T. D. Nguyen, C. M. Yakacki, P. D. Brahmbhatt, M. L. Chambers, Modeling the relaxation mechanisms of amorphous shape memory polymers, Advanced Materials 22 (31) (2010) 3411–3423.

[47] J. D. Ferry, J. D. Ferry, Viscoelastic properties of polymers, John Wiley & Sons, 1980.

[48] K. Kamrin, E. Bouchbinder, Two-temperature continuum thermomechanics of deforming amorphous solids, Journal of the Mechanics and Physics of Solids 73 (2014) 269–288.

[49] T. M. Nieuwenhuizen, Thermodynamics of the glassy state: effective temperature as an additional system parameter, Physical review letters 80 (25) (1998) 5580.

[50] B. D. Coleman, M. E. Gurtin, Thermodynamics with internal state variables, The Journal of Chemical Physics 47 (2) (1967) 597–613.

[51] A. Adams, C. Buckley, D. Jones, Biaxial hot drawing of poly(ethylene terephthalate): measurements and modelling of strain-stiffening, Polymer 41 (2) (2000) 771 – 786. doi:https://doi.org/10.1016/S0032-3861(98)00834-9.
URL http://www.sciencedirect.com/science/article/pii/S0032386198008349

[52] S. Reese, S. Govindjee, A theory of finite viscoelasticity and numerical aspects, International Journal of Solids and Structures 35 (26) (1998) 3455 – 3482. doi:https://doi.org/10.1016/S0020-7683(97)00217-5.
URL http://www.sciencedirect.com/science/article/pii/S0020768397002175

[53] A. Dawson, M. Rides, C. Allen, J. Urquhart, Polymer–mould interface heat transfer coefficient measurements for polymer processing, Polymer Testing 27 (5) (2008) 555–565.

[54] X. Xu, A. Needleman, Void nucleation by inclusion debonding in a crystal matrix, Modelling and Simulation in Materials Science and Engineering 1 (1999) 111.

[55] R. Fraser, I. Ward, Temperature dependence of craze shape and fracture in polycarbonate, Polymer 19 (2) (1978) 220 – 224. doi:https://doi.org/10.1016/0032-3861(78)90043-5.
URL http://www.sciencedirect.com/science/article/pii/0032386178900435

[56] M. Wendlandt, T. A. Tervoort, U. Suter, Strain-hardening modulus of cross-linked glassy poly(methyl methacrylate), Journal of Polymer Science Part B: Polymer Physics 48 (2010) 1464 – 1472. doi:10.1002/polb.21979.

[57] R. Dupaix, M. C. Boyce, Finite strain behavior of poly(ethylene terephthalate) (pet) and poly(ethylene terephthalate)-glycol (petg), Polymer 46 (2005) 4827–4838. doi:10.1016/j.polymer.2005.03.083.

[58] H. van Melick, L. Govaert, H. Meijer, On the origin of strain hardening in glassy polymers, Polymer 44 (2003) 2493–2502. doi:10.1016/S0032-3861(03)00112-5.

[59] A. J. Kinloch, C. C. Lau, J. G. Williams, The peeling of flexible laminates, International Journal of Fracture 66 (1) (1994) 45–70. doi:10.1007/BF00012635.
URL https://doi.org/10.1007/BF00012635

[60] K.-S. Kim, J. Kim, Elasto-plastic analysis of the peel test for thin film adhesion, Journal of Engineering Materials and Technology 110 (3) (1988) 266–273.
URL http://dx.doi.org/10.1115/1.3226047

[61] E. Breslauer, T. Troczynski, Determination of the energy dissipated during peel testing, Materials Science and Engineering: A 302 (1) (2001) 168 – 180. doi:https://doi.org/10.1016/S0921-5093(00)01370-8.
URL http://www.sciencedirect.com/science/article/pii/S0921509300013708

[62] J. Guo, R. Xiao, H. S. Park, T. D. Nguyen, The temperature-dependent viscoelastic behavior of dielectric elastomers, Journal of Applied Mechanics 82 (9) (2015) 091009.

[63] V. Tvergaard, J. W. Hutchinson, The relation between crack growth resistance and fracture process parameters in elastic-plastic solids, Journal of the Mechanics and Physics of Solids 40 (6) (1992) 1377 – 1397.

[64] R. Xiao, T. D. Nguyen, A thermodynamic modeling approach for dynamic softening in glassy amorphous polymers, Extreme Mechanics Letters 8 (2016) 70–77.

[65] I. Georgiou, H. Hadavinia, A. Ivankovic, A. J. Kinloch, V. Tropsa, J. G. Williams, Cohesive zone models and the plastically deforming peel test, The Journal of Adhesion 79 (3) (2003) 239–265. arXiv:https://doi.org/10.1080/00218460309555, doi:10.1080/00218460309555.
URL https://doi.org/10.1080/00218460309555

[66] P. Pan, B. Zhu, Y. Inoue, Enthalpy relaxation and embrittlement of poly(l-lactide) during physical aging, Macromolecules 40 (26) (2007) 9671– 9664. doi:doi:10.1021/ma071737c.
URL https://doi.org/10.1021/ma071737c

[67] A.-M. Yang, R. Wang, J. Lin, Ductile-brittle transition induced by aging in poly(phenylene oxide) thin films, Polymer 37 (25) (1996) 5751 – 5754. doi:https://doi.org/10.1016/S0032-3861(96)00395-3.
URL http://www.sciencedirect.com/science/article/pii/S0032386196003953

[68] R. J. M. Smit, W. A. M. Brekelmans, H. E. H. Meijer, Predictive modelling of the properties and toughness of polymeric materials part i why is polystyrene brittle and polycarbonate tough?, Journal of Materials Science 35 (11) (2000) 2855–2867. doi:10.1023/A:1004711622159.
URL https://doi.org/10.1023/A:1004711622159

[69] W. A. Spitzig, O. Richmond, Effect of hydrostatic pressure on the deformation behavior of polyethylene and polycarbonate in tension and in compression, Polymer Engineering & Science 19 (16) (1979) 1129–1139. arXiv:https://onlinelibrary.wiley.com/doi/pdf/10.1002/pen.760191602, doi:10.1002/pen.760191602.
URL https://onlinelibrary.wiley.com/doi/abs/10.1002/pen.760191602

[70] M. L. Manning, J. S. Langer, J. M. Carlson, Strain localization in a shear transformation zone model for amorphous solids, Phys. Rev. E 76 (2007) 056106. doi:10.1103/PhysRevE.76.056106.
URL https://link.aps.org/doi/10.1103/PhysRevE.76.056106

[71] E. Bouchbinder, J. S. Langer, Nonequilibrium thermodynamics of driven amorphous materials. ii. effective-temperature theory, Phys. Rev. E 80 (2009) 031132. doi:10.1103/PhysRevE.80.031132.
URL https://link.aps.org/doi/10.1103/PhysRevE.80.031132

[72] W. Dettmer, S. Reese, On the theoretical and numerical modelling of armstrong–frederick kinematic hardening in the finite strain regime, Computer Methods in Applied Mechanics and Engineering 193 (1) (2004) 87 – 116. doi:https://doi.org/10.1016/j.cma.2003.09.005.
URL http://www.sciencedirect.com/science/article/pii/S0045782503005218

[73] F. Schwarzl, A. Staverman, Higher approximation methods for the relaxation spectrum from static and dynamic measurements of visco-elastic materials, Applied Scientific Research, Section A 4 (2) (1953) 127–141.

[74] P. Haupt, A. Lion, E. Backhaus, On the dynamic behaviour of polymers under finite strains: constitutive modelling and identification of parameters, International Journal of Solids and Structures 37 (26) (2000) 3633–3646.

[75] C. Lindsey, G. Patterson, Detailed comparison of the williams–watts and cole–davidson functions, The Journal of chemical physics 73 (7) (1980) 3348–3357.